University of Bergen

Master Thesis

Neutral Pion Production in p–Pb Collisions at $\sqrt{s_{\mathrm{NN}}} = 5.02$ TeV with ALICE PHOS at the LHC

Author:
Hongsheng Zhu

Supervisor:
Prof. Dieter Röhrich
Prof. Daicui Zhou
Dr. Constantinos Loizides

A thesis submitted in fulfilment of the requirements for the degree of Master in Physics

in the

Department of Physics and Technology

August 2015

UNIVERSITY OF BERGEN

Abstract

Department of Physics and Technology

Master in Physics

Neutral Pion Production in p–Pb Collisions at $\sqrt{s_{\mathrm{NN}}}$ = 5.02 TeV with ALICE PHOS at the LHC

by Hongsheng ZHU

In this thesis, the neutral mesons measurement with ALICE PHOS at the LHC is presented. Depending on the technical design of PHOS and its momentum reach, the strategies of the neutral mesons extraction by invariant mass analysis are studied. The main reason is due to the detector granularity. Clusters start to merge and maybe misidentified as single cluster in high multiplicity environment, as well as for high p_{T} π^0. Cluster unfolding algorithm and shower shape parameters allow us to separate γ and π^0 at high p_{T}.

From current statistics with p–Pb collisions at $\sqrt{s_{\mathrm{NN}}} = 5.02$ T eV , ~ 90 million min-bias events are analyzed. By using the invariant mass analysis, π^0 spectrum is extracted to a p_{T} range of 25 GeV/c with PHOS. For the corrections of the raw spectrum, we take into account the geometrical acceptance and the reconstruction efficiency together by official DPMJET simulations. The final π^0 invariant yield are obtained with good matching with other three individual analysis.

Acknowledgements

For the ancestors who paved the path before me upon whose shoulders I stand. This is dedicated to my family and the many colleagues who supported me on this journey. Thank you.

I would like to give my deepest gratitude to my supervisors Professor Dieter Röhrich, Doctor Constantinos Loizides and Professor Daicui Zhou for their unwavering support, collegiality, and mentorship throughout this project.

I would like to extend my thanks to those who offered collegial guidance and support over years: Doctor Xiaoming Zhang, Doctor Xiangrong Zhu, Doctor Jason Kamin, Master Friederike Bock.

Contents

List of Figures

List of Tables

To my lovely family, to the moon and the sun...

Chapter 1

Introduction

Searching for the elementary building blocks of the physical world has always been a central theme in the history of scientific research. The theories and experimental discoveries since the 1930s have demonstrated that everything in the universe is made from a few basic building blocks called fundamental particles, governed by four fundamental forces. Even thought the Standard Model of particle physics is the most experimentally successful theory there is of the subatomic world, it does not explain the complete picture. To fulfill the picture, the currently largest accelerator, The Large Hadron Collider (LHC)[1], has been constructed at the European Organization for Nuclear Research (CERN).

The accelerator was commissioned in 2009 and reached new energy frontiers with the highest center of mass energy $\sqrt{s} = 8$ TeV in the pp and $\sqrt{s_{\mathrm{NN}}} = 2.76$ TeV in Pb–Pb collisions. It is still expected to reach the maximum designed energy of $\sqrt{s} = 14$ TeV in the near future. The LHC first research run (2010-2013) delivered many exciting results. Among those the most celebrated one is the discovery of the Higgs like boson by ATLAS[2] and CMS[3] experiments. After two years shutting down for upgrades, the second research run commenced with collision energy of $\sqrt{s} = 13$ TeV on 3 June 2015.

Beside the research in the electroweak sector, LHC experiments are also designed to study the strongly interacting matter and its phase transition. The Quantum Chromodynamics (QCD) is known to be the only gauge theory where phase transition is reachable experimentally. High temperatures and densities reached in the ultra-relativistic nuclear collisions give rise to the medium of deconfined quarks and gluons, called Quark Gluon Plasma (QGP)[4] and this is the main objective of study of the ALICE[5], one of the four major LHC experiments.

This thesis focus on the measurement of the neutral pion production in p–Pb collisions in ALICE. The π^0 yeild is reconstructed based on invariant mass of photon pairs captured in PHOton Spectrometer (PHOS). The measurement of the neutral pion production in p–Pb collisions provides the information about the nuclear modified parton distribution function and allows to disentangle initial-state effects and final-state effects for Pb–Pb collisions. Meanwhile, it is also important to understand the decay photon background in measuring the direct photon production.

This thesis is organized as follows: Chapter 1 provides introduction into the physics of the conducted analysis. The following chapter 2 introduces the LHC machine and the ALICE experiment. The π^0 reconstruction via two-photon decays is described in details in chapter 3. Finally the results and outlooks is concluded in chapter 4.

1.1 Standard Model and QCD

The Standard Model (SM)[6–8] of particle physics is a gauge Quantum Field Theory (QFT)[9] describing the fundamental building blocks of matter and their interactions including the electromagnetic, weak, and strong nuclear interaction. To our current knowledge, elementary particles include quarks and leptons in three generations as well as four gauge bosons and Higgs boson, which act as "force carrier particles" that mediate interactions among fermions(Figure 1.1). By the time the electromagnetic and weak interactions are unifiedly explained by electro-weak theory, Quantum Chromodynamics (QCD) [10] has been established as QFT for characterizing the properties of the strong interaction, which describes the interaction between quarks and gluons(Table 1.1).

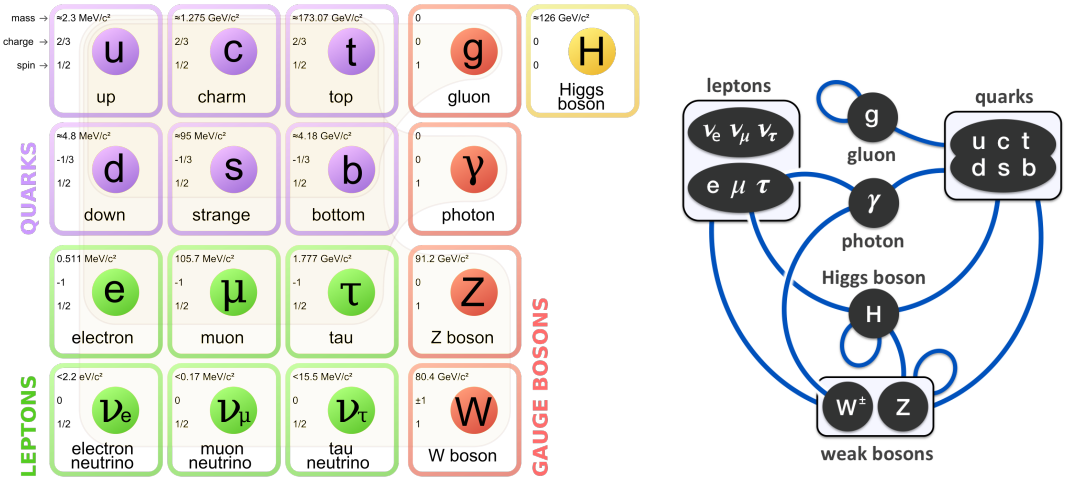

FIGURE 1.1: Elementary particles in the Standard Model (left) and the fundamental interactions between them (right) [11]

Interactions	Gauge boson(s)	Applies to
electromagnetic	photon (γ)	charged particles
weak	$W^{\pm}$ and Z^0	quarks and letpons
strong	8 gluons (g)	quarks

TABLE 1.1: Fundamental forces and their carries in the Standard Model [12]

As a part of Standard Model, QCD is the best theory describing the behavior of nuclear matter which is made of quark and gluon via the strong color force. It obeys to the principles of a relativistic QFT with a non-Abelian gauge invariance $SU(3)_c$. The Lagrangian in QCD is given by

$$\mathcal{L}_{QCD} = \bar{\psi}_i(i\gamma_\mu D^\mu_{ij} - m\delta_{ij})\psi_j - \frac{1}{4}G^a_{\mu\nu}G^{\mu\nu}_a \tag{1.1}$$

with gauge covariant derivative

$$D^\mu = \partial^\mu - i\mathcal{A}^\mu \tag{1.2}$$

and gauge invariant gluon field strength tensor

$$G^a_{\mu\nu} = \partial_\mu \mathcal{A}^a_\nu - \partial_\nu \mathcal{A}^a_\mu + g_s f^a_{bc}\mathcal{A}^b_\mu \mathcal{A}^c_\nu \tag{1.3}$$

where $\mathcal{A}^a_\mu(x)$ represents the quark field, g_s is the effective strong charge and $\mathcal{A}^a_\mu$ is a gluon field, while γ_μ are Dirac γ-matrices. Different techniques have been developed to deal with it, such as perturbative QCD (pQCD), lattice QCD, Ads/CFT, effective field theory etc.

The last non-Abelian term in Equation 1.3 represents the gluon self-interaction. It introduces a very important property of QCD, the Asymptotic Freedom, which explains why quarks are born free but everywhere they're in chain.

1.1.1 Asymptotic freedom

Asymptotic freedom is a feature of QCD that causes bonds between particles to become asymptotically weaker as energy increases and distance decreases. The coupling constant of QCD is given by $\alpha_s = g_s^2/4\pi$, which is much larger than $\alpha_{em} \backsimeq 1/137$ in QED. The values of α_s cannot be predicted by QCD but needs to be determined from experiments. The dependence of α_s on momentum transfer (Q) in leading order can be expressed by

$$\alpha_s(Q) \approx \frac{12\pi}{(33 - 2N_f)ln(Q^2/\Lambda^2_{QCD})} \tag{1.4}$$

where N_f is the number of flavors and Λ_{QCD} is non-perturbative scale of QCD (Figure 1.2).

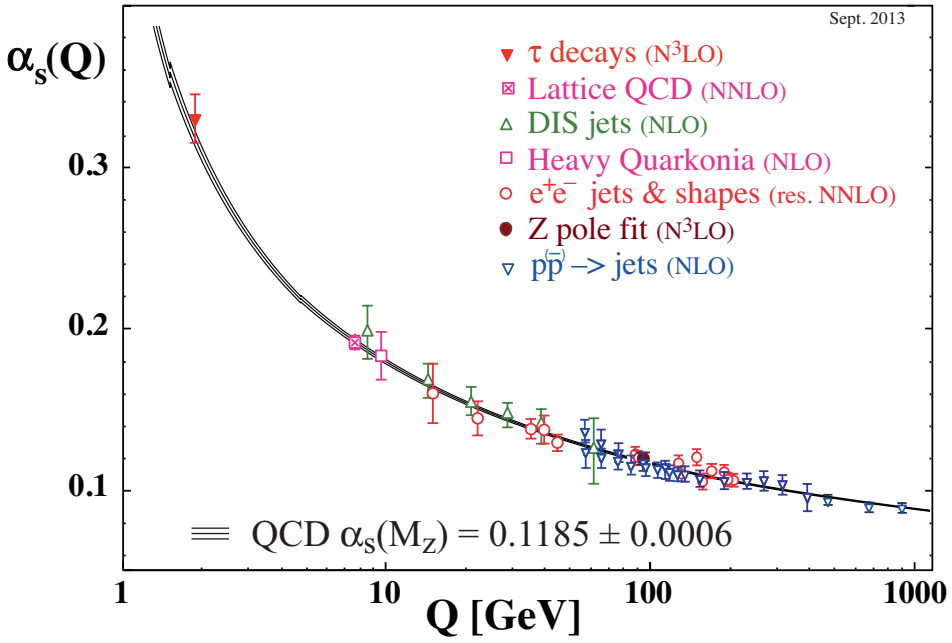

FIGURE 1.2: Summary of measurements of α_s as a function of the momentum transfer Q. The respective degree of QCD perturbation theory used in the extraction of α_s is indicated in brackets (NLO: next-to-leading order; NNLO: next-to-next-to leading order; res. NNLO: NNLO matched with resumed next-to-leading logs; N^{3}LO: next-to-NNLO)[13].

The phenomenological potential between a $q\bar{q}$ pair as a function of radial distance (r) between them can be approximated by:

$$V_s = -\frac{4}{3}\frac{\alpha_s}{r} + \kappa r \tag{1.5}$$

where κ is the string tension. For smaller r the first term dominates, and it is equivalent to a Coulomb-like interaction. As r increases, the potential grows linearly, and consequently the energy to take out a quark from a hadron should be infinite. At some point it becomes energetically more favorable to create a new $q\bar{q}$ pair (a meson) from the vacuum. This behavior at long-distances is called confinement and is the reason why single quarks are never observed in nature.

Equation 1.4 reveals that, due to the small value of Q^2 in normal world, the coupling between quarks and gluons is very strong since they are confined in the hadrons. On the contrary, for processes with large momentum transfer, α_s becomes small, free quarks and gluons behave as free particles in the QCD vacuum: this is the well known "asymptotic freedom" (or deconfinement). Furthermore, the Chiral Symmetry in the QCD

Lagrangian, Equation 1.1, will be broken in this processes. And it is the reason why matters have mass.

1.1.2 Quark gluon plasma

The idea of asymptotic freedom as discussed in Section 1.1.1, which is strong at large separations, weakens as the quarks get closer to one another has a fascinating consequence. When temperatures or densities become very high, strongly interacting quarks and gluons become free and transform themselves into a new, deconfined phase of matter, for which the term 'quark gluon plasma (QGP)' was coined. And it is thought to have permeated the first microseconds after the Big Bang.

While the perturbative-QCD calculations fail to describe the phase transition between hadronic matter and QGP due to particle correlations in long distance, a new gauge theory, Lattice QCD, was proposed by K. Wilson[14] in 1974 to solve the QCD theory of quarks and gluons in non-perturbative approach. The pressure is given in the Stefan-Boltzmann form[15, 16]

$$p = cT^4[1 - a(\frac{m_{th}}{T})^2] = cT^4[1 - ag^2(T)] \tag{1.6}$$

and the energy density

$$\epsilon = 3cT^4[1 - ag^2(T) - \frac{2am_{th}}{3}(\frac{dg}{dT})] \tag{1.7}$$

where c and a are color and flavor dependent and m_{th} is an effective thermal mass of quarks and gluons. As shown in Figure 1.3a, the ϵ/T^4 changes sharply at above the critical temperature, and from Figure 1.3b we can see that there are still some strong interaction region between $T_c < T < 2T_c$. Because there are no dimensional parameters in QCD with the limit of massless quarks, the value of transition temperature only can be determined by some other physics observables. Lattice QCD gets this value of $T_c = 190 \pm 10$ MeV by fine structure charmonium calculation[17]. Latest conclusion from experiment results present the critical temperature for the QCD phase transition is $175 \pm \frac{1}{7}$ MeV[18].

So we get the conclusion that above the critical energy $170 \sim 200$ MeV and a energy density above 1 GeV/fm^3, the deconfinement could occur abruptly[19].

A schematic view of the QCD phase diagram of hadronic matter including the QGP can be seen in Figure 1.4.

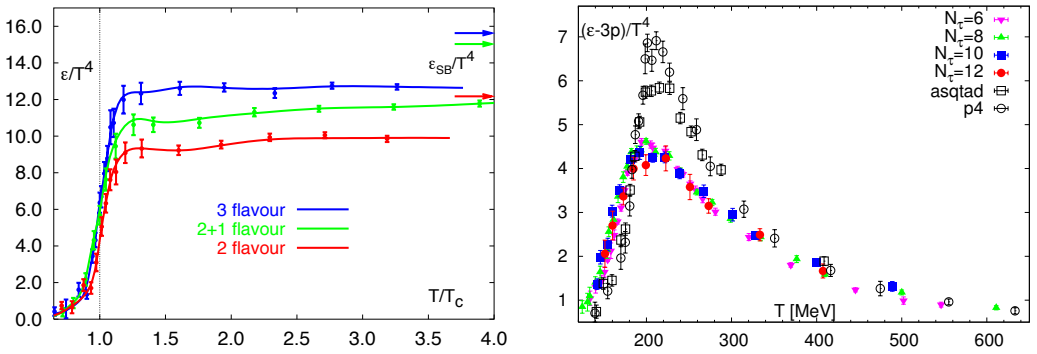

(A) Energy density[20] (B) Interaction measurement $((\epsilon - 3p)/T^4)$[17]

FIGURE 1.3: The energy density from lattice QCD calculation.

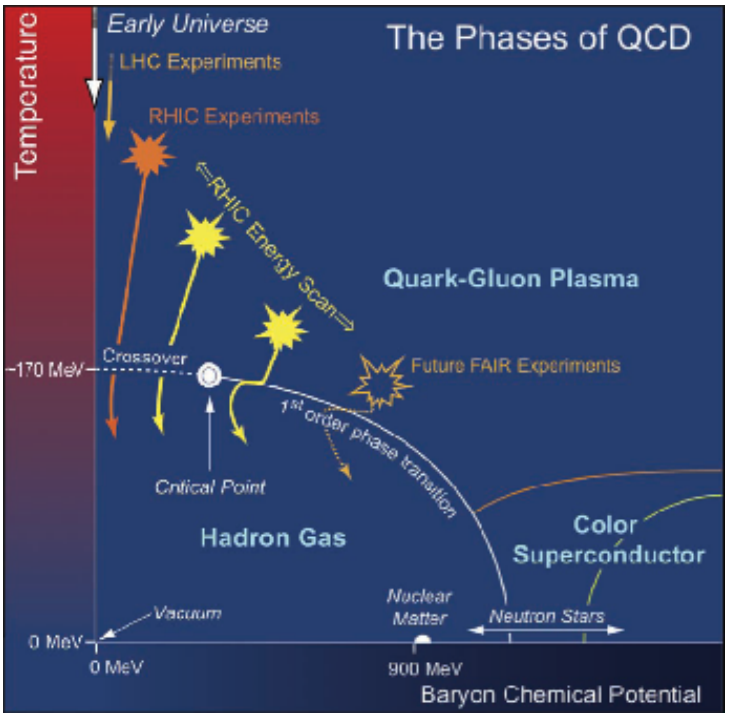

FIGURE 1.4: Schematic of the QCD phase diagram of nuclear matter in terms of the temperature (T) versus baryon chemical potential (μ_B)

- At low temperature (zero temperature) and high chemical potential (at a few times than nuclear matter), the attractive interactions between quarks will lead to the formation of the colored bosonic diquark pairs and Cooper pairs of QCD from deconfined phase. So that the diquarks condense at low temperature to become a color superconductor.

- At intermediate temperature and low chemical potential, a first order phase transition from hadronic matter to plasma will happen with typical properties of deconfinement and chiral symmetry restoration.

- Critical point is an end point of first order and a start point of second order, which is one of our main goals both for theory and experiment.
- At extreme high temperature and almost zero chemical potential, some arguments think it as a second order phase transition, while others show the evidences as a crossover with a smooth and continuous transition.

It is believed that collisions of protons or electrons do not produce high enough particles densities to create QGP. Heavy-ion collisions, on the other hand, seem to be a good candidate for the production of a QGP state, at least if the energy of the colliding nuclei is large enough. The experiments at the LHC (ALICE, ATLAS and CMS) are moving on the TeV era to address the questions above. ALICE is one of the main experiments designed for the heavy-ion collisions at $\sqrt{s_{\mathrm{NN}}} = 5.5$ TeV. It will step into extreme high energy and density with almost zero chemical potential, where the phase transition from hadronic matter to plasma is expected to take place.

1.2 Heavy ion physics

High-energy nuclear physics studies the behavior of nuclear matter in energy regimes typical of high energy physics. The primary focus of this field is the study of heavy-ion collisions, as compared to lower atomic mass atoms in other particle accelerators.Ultra-Relativistic Heavy Ion Collisions(URHIC) is an unique way to produce the QGP in laboratory.

1.2.1 Heavy ion collisions

A schematic view of the time evolution of the heavy-ion collision is shown in Figure 1.5 and it follows

1. Initial collisions and the formation of the “fireball” in limited space-time volume;
2. Deconfinement evolved from pre-equilibrium to thermal QGP;
3. Transition from thermal QGP to chemical equilibrium, as well as a mixed phase. It produces transient massive effective quarks, while free gluons are disappearing;
4. Hadronization, when quarks are combined into hadrons with the effective and strong interaction. Then the unstable hadrons will decay into stable and final detectable particles.

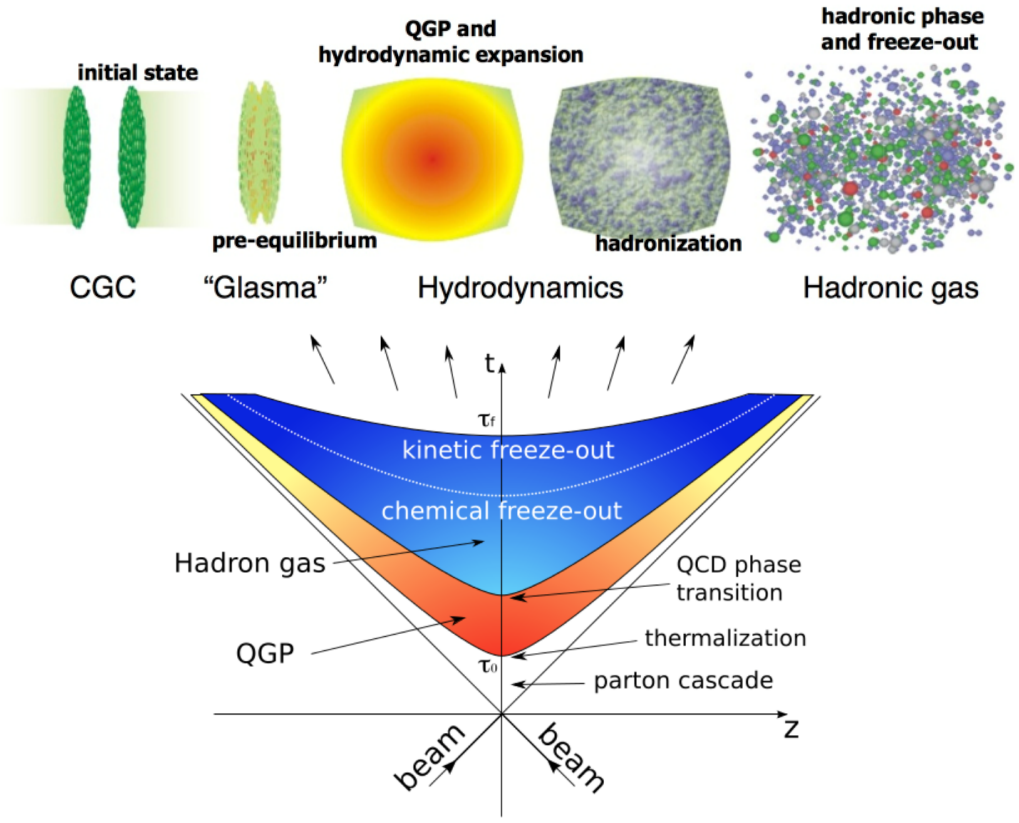

FIGURE 1.5: Top: Overview of the space-time evolution in a ultra-relativistic nuclear collision. Bottom: Schematic representation of the various stages of a heavy ion collision as a function of time t and the longitudinal coordinate z (the collision axis)

Due to the size of the nuclei, the collision of two nuclei is not necessarily head on. The overlap region (dependent on the impact parameter) of the two nuclei, which contains nucleons that actually collide, can range from full overlap (central collision) to minimal overlap (peripheral collision). With the help of Glauber model, the collisions are then sorted in centrality percentiles[21].

1.2.2 Search for QGP

The search for QGP signatures began at Berkeley Bevalac, continued at AGS[1] accelerator at Brookhaven National Laboratory and at SPS[2] at CERN with $\sqrt{s_{\mathrm{NN}}} = 4.6$ GeV and 17.2 GeV per colliding nucleon pair respectively (Table 1.2). The results at SPS provided hints of QGP existence, although some alternative explanations for the SPS observations, discussed below, were offered leaving some of heavy ion physicists unconvinced. Nevertheless, CERN announced discovery of the new state of matter in the spring 2000[22].

[1] Alternating Gradient Synchrotron (AGS)
[2] Super Proton Synchrotron (SPS)

Operate	Machine	Facility	Max $\sqrt{s_{\mathrm{NN}}}$
1971	Bevalac	LBNL	∼2 GeV
1975	UNIAC	GSI	∼2 GeV
1986	AGS	BNL	∼5 GeV
1986	SPS	CERN	∼20 GeV
1990	SIS	GSI	∼2 GeV
1994	SPS	CERN	∼17 GeV
2000	RHIC	BNL	200 GeV
2010	LHC	CERN	2.76 TeV

TABLE 1.2: List of center of mass energies (per nucleon) for recent accelerators.

The main experimental evidences for the observation of the new state of matter at SPS were based for example on the observation of the low-mass dilepton enhancement[23], quarkonia suppression[24, 25] or strangeness enhancement[26, 27]. For example the dilepton mass spectrum is shown on the left panel of Figure 1.6. The measured distribution is compared to the hadronic cocktail, the sum of all contributions from know hadronic decays. An excess between π and ρ/ω mass range is interpreted as a partial restoration of the chiral symmetry in QGP[28]. These observations certainly support the expected trends induced by QGP. On the other hand, there were observations like high p_{T} π^0 production at $\sqrt{s_{\mathrm{NN}}}$ = 17 GeV S–S and Pb–Pb data by WA80[29] and WA98[30] experiments (right panel of Figure 1.6). The solid lines represent the expectation from the pQCD calculations scaled up by number of binary collisions. The deconfined opaque medium is expected to suppress the high p_{T} particle yield (discussed in details in Section 1.3.1). This is, however, not seen on the right panel of Figure 1.6 where the measured data (solid black symbols) show no sign of suppression as compared to scaled pQCD calculation (solid lines)[31].

The first results from Relativistic Heavy Ion Collider (RHIC) at BNL surprised everybody by strikingly large suppression of hard particle production in central Au–Au $\sqrt{s_{\mathrm{NN}}}$ = 130 GeV collisions[32]. More recent data[33, 34] are shown on Figure 1.7. The observation of jet quenching was a strong hint towards confirmation of the QGP existence. Yet it was not clear until four years later, when results from the control d–Au run at RHIC proved that the suppression is not an initial state effect, the Color Glass Condensate(CGC) picture see e.g.[35]. Nowadays the suppression is understood as suppression by induced gluons radiation e.g.[36–40] and many others. The p–A runs are a crucial reference to the measurements conducted in heavy ion collisions, which provide access to initial and "cold" nuclear matter effects. Another important results that support the QGP formation at RHIC are observation of flow of the medium[41, 42] or studies of direct photon yield[43, 44].

The nuclear modification factor R_{AA} shows a dramatic suppression in heavy ion collisions

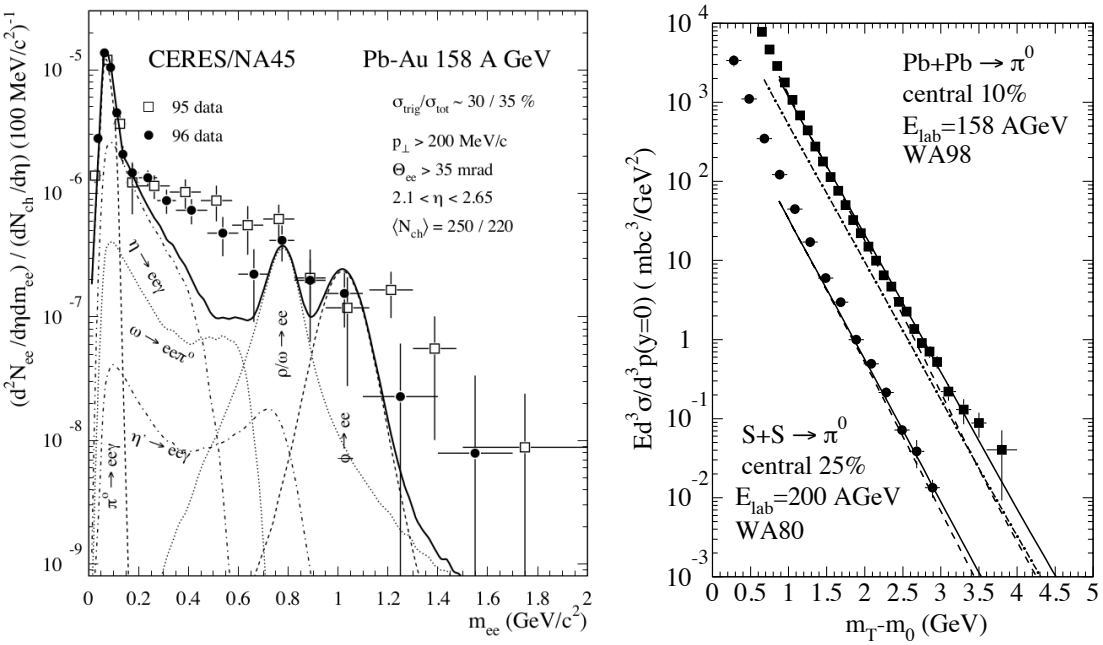

FIGURE 1.6: Left: e^+e^- mass spectrum from CERES/NA45 experiment[45]. The data are compared to the sum of the expected contributions from hadron decays (solid line). An excess in the low mass region is interpreted to be due to the (partial) chiral symmetry restoration in QGP. Right: Single-inclusive π^0 spectra in central S + S at E_{lab} = 200 GeV (WA80) and Pb + Pb collisions at E_{lab} = 158 GeV (WA98)[31]. The solid and dashed lines represent the pQCD expectations. Existence of opaque QGP should lead to a suppression of the high-p_T yield wrt pQCD scaled expectations contrary to the data.

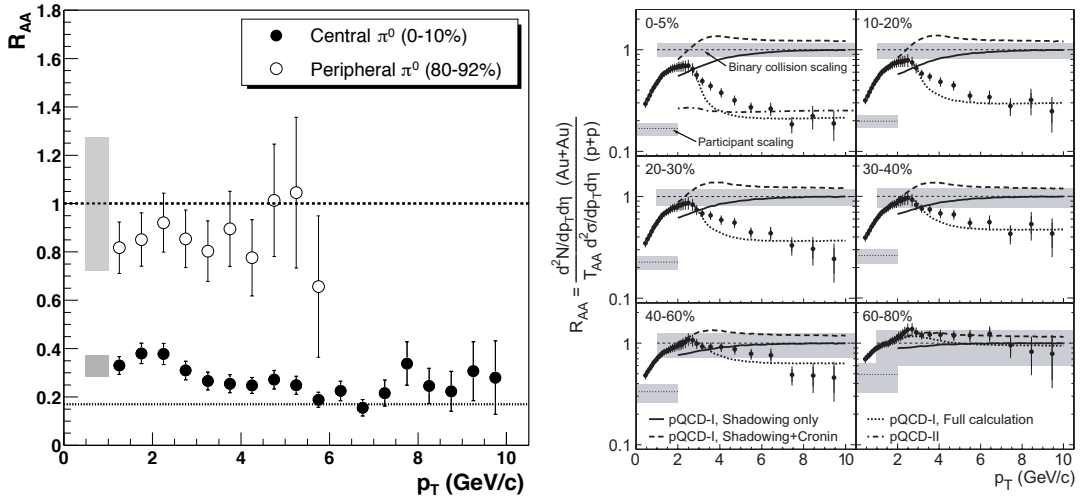

FIGURE 1.7: Left: Nuclear modification factor $R_{AA}(p_T)$ for π^0 in central (closed circles) and peripheral (open circles) Au+Au at $\sqrt{s_{NN}}$ = 200 GeV[32]. Right: $R_{AA}(p_T)$ for $(h^+ + h^-)/2$ in $|\eta| < 0.5$, for centrality-selected Au+Au spectra relative to the scaled p+p spectrum[34].

with respect to the pp baseline expectation presumably due to the formation of QGP. However, in order to disentangle how much of this phenomenon is simply a result of effects from "cold" nuclear matter in the initial state, p–A collisions are a necessary and useful control measurement. It's my motivation to study the π^0 yield in p–Pb collisions in ALICE at LHC.

1.3 Nuclear matter effects

Presence of nuclear medium around the point of a hard scattering event results in interaction of the products of the hard scattering with the matter. The initial conditions before the hard scattering can also be altered. In case of the strongly interacting hot and dense QGP, the propagating partons can radiate gluons in vicinity of scattering centers, which is called induced gluon radiation[46]. Mean energy loss of a parton in medium can then be described by the medium transport coefficient[47]. For the heavier quarks, energy loss from elastic re-scattering needs to be also considered. Nuclear effects can also arise from presence of "cold" nuclear matter. For example initial state effects as shadowing and anti-shadowing[48] or Cronin[49] effect have been observed in p–A or d–A collisions. When observing modifications in between pp and A–A collisions, it is important to study the effects of cold nuclear matter as well, to be able to correctly disentangle the initial and final state modifications.

1.3.1 Jet quenching

The partons propagating through medium lose energy, their p_{T} is lowered. The energy loss then demonstrates as suppression of final state p_{T} hadrons (jet quenching). The effect energy loss in the inclusive transverse spectra can be quantified with nuclear modification factor

$$R_{AA}(p_{\mathrm{T}}) = \frac{d^2N/dp_{\mathrm{T}}dy|_{AA}}{\langle T_{AA}\rangle d^2\sigma/dp_{\mathrm{T}}dy|_{pp}} \tag{1.8}$$

where the nuclear overlap function $\langle T_{AA}\rangle$ is related to the average number of inelastic nucleon-nucleon collisions as $\langle T_{AA}\rangle = \langle N_{coll}\rangle/\sigma^{pp}_{inel}$. N_{coll} is a scaling of binary collisions based on Glauber modeling[21]. $R_{AA} = 1$ represents no modificaiton by nuclear matter. R_{pA} is defined analogically.

The nuclear modification factor can be constructed for final state particles which come from processes that are affected by the interaction with medium same as for particles which are expected to traverse the medium without interacting with it, for example photons. Observation of R_{AA} for various particle species is shown on Figure 1.8. A

large suppression of production of hadrons in central A–A collisions is observed. Also the photon and intermediate vector boson yields seen unchanged.

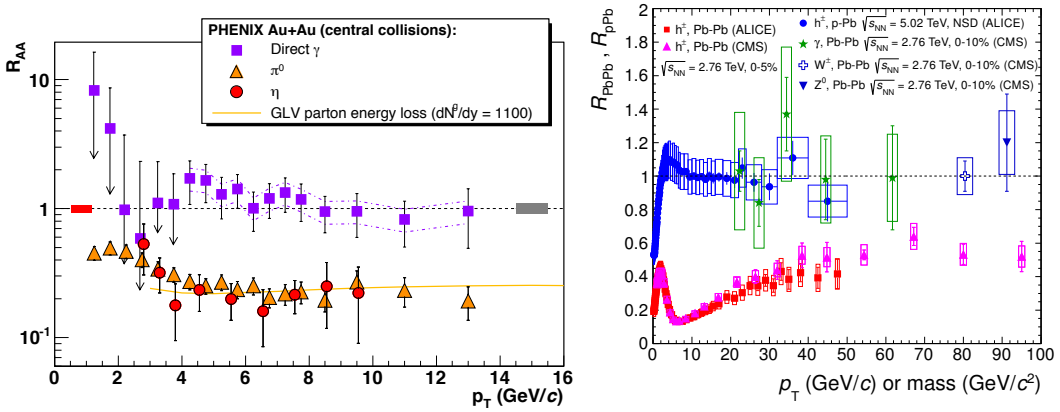

FIGURE 1.8: Left: $R_{AA}(p_{\mathrm{T}})$ measured in central Au+Au at $\sqrt{s_{\mathrm{NN}}}$ = 200 GeV for η, π^0 and direct γ[50]. The pp reference for γ measurement is NLO calculation. The solid yellow curve is a parton energy loss prediction. Right: Transverse momentum dependence of the nuclear modification factor R_{pPb} of charged particles ($h^{\pm}$) measured in minimum-bias (NSD) p–Pb collisions in comparison to data on the nuclear at $\sqrt{s_{\mathrm{NN}}}$ = 5.02 TeV[51].

Two particle correlation method also provides a good handle to study the jet quenching. The yields of particles associated to a high p_{T} trigger are studied in azimuth (or rapidity) e.g. by PHENIX[32]. The azimuthal hadronic correlation produce a specific function shape (Figure 1.9). The shape originates from the fact that due to the in medium energy loss it is likely that a high p_{T} hadron originates from a hard scattering close to medium surface[52]. The recoiling (away side, $\Delta\phi = \pi$) jet is expected to traverse the medium and get quenched more that the trigger one (near side, $\Delta\phi = 0$). Vanishing of the away side yields is another sign of energy loss induced by medium.

The correlated yields I_{AA} (Equation 1.9) can be constructed as ratio of near or away side yields Y in A–A and pp collisions

$$I_{AA} = \frac{Y^{AA}(p_{T,assoc},\eta)|_{p_{T,trigg}}}{Y^{pp}(p_{T,assoc},\eta)|_{p_{T,trigg}}} \tag{1.9}$$

1.3.2 Cold nuclear matter effects

Cold Nuclear Matter (CNM) effects[55] cause to enhance the particle production by multiple soft scattering, and/or make modification of the parton distribution functions in the initial state. Many mechanisms are introduced to describe these effects. For instance, followings are known as the initial state effects.

One of the initial state CNM effects is the so called k_T-broadening[56]. It is a consequence of the fact that before the inelastic interaction, partons of the projectile nucleon could

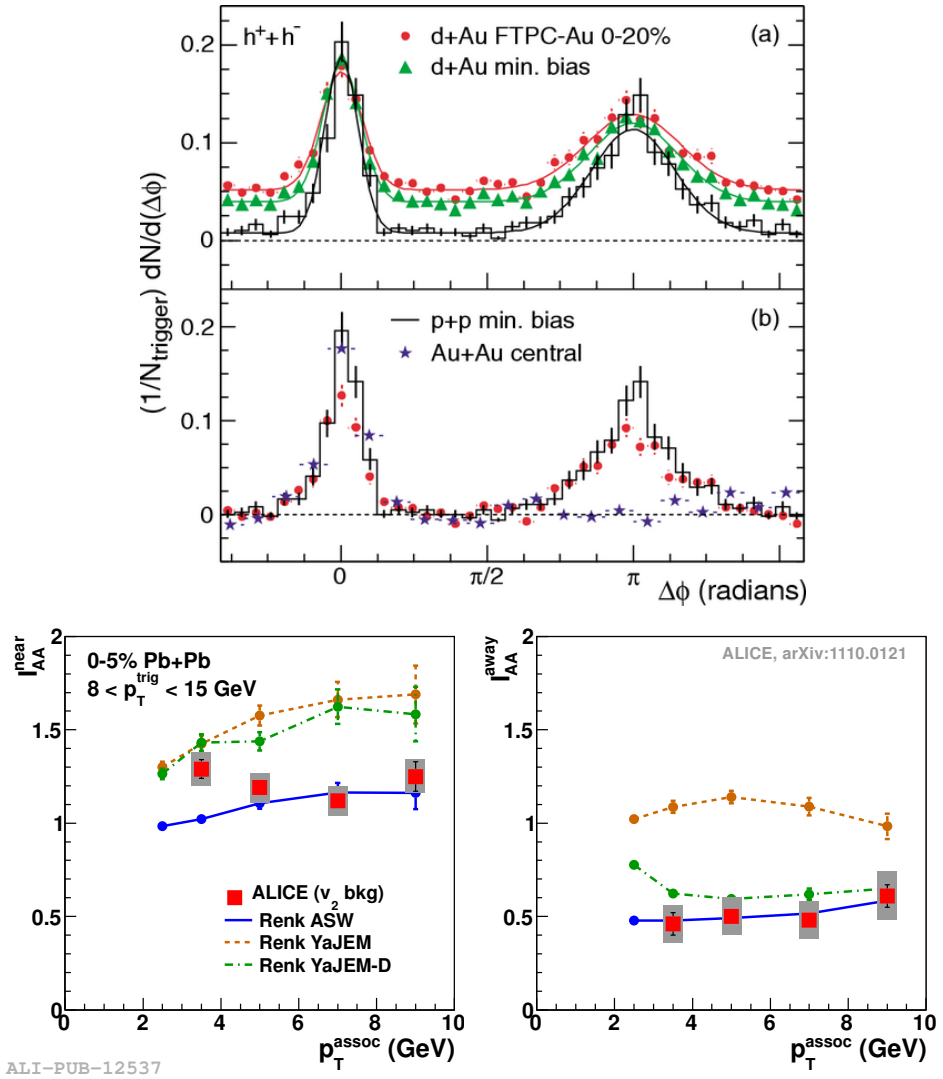

FIGURE 1.9: (a) Efficiency corrected two-particle azimuthal distributions for minimum bias and central d–Au collisions, and for pp collisions. (b) Comparison of two-particle azimuthal distributions for central d–Au collisions to those seen in pp and central Au–Au collisions[53]. (c),(d) Charged hadron I_{AA}, $p_{T,trigg}$ = 8-15 GeV (background subtraction: v2)[52, 54]. Near side (c), away side (d).

have suffered multiple elastic scatterings in the target nucleus. These interactions lead to a small extra p_{T} component of the parton, which reflects in the p_{T}-distribution of the particles produced in the hard scattering of this parton, in the case of A–A or p–A collisions.

This k_T-broadening explains the observed Cronin enhancement, which was seen for first time in p–A collisions at Fermilab[57, 58]. This experimental observation is an increased yield in p–A collisions at intermediate p_{T} compared to binary scaled yield in pp collisions. Since this extra-k_T becomes less relevant with increasing hadron p_{T}, the Cronin enhancement should disappear as $p_{\mathrm{T}} \to \infty$. For the same reason it should become

weaker as psNN increases. In the left panel of Figure 1.10 the Cronin enhancement (R_{AA} larger than unity at intermediate p_{T}) is shown in d–Au collisions at top RHIC energy.

Another known initial state effect is the nuclear modification of the parton distribution functions (PDF) in a nucleus with respect to those of the proton. This modification depends on Bjorken x (see Appendix B for Bjorken scaling definition) and Q^2. In particular at low x (partons with $x < 10^{-2}$) a reduction of the PDFs is observed, usually called shadowing, as it is shown in the right panel of Figure 1.10 [59]. In particular, the shadowing affects significantly the measured value of R_{AA} at low p_{T}. The shadowing region can be described phenomenologically by gluon saturation at small x.

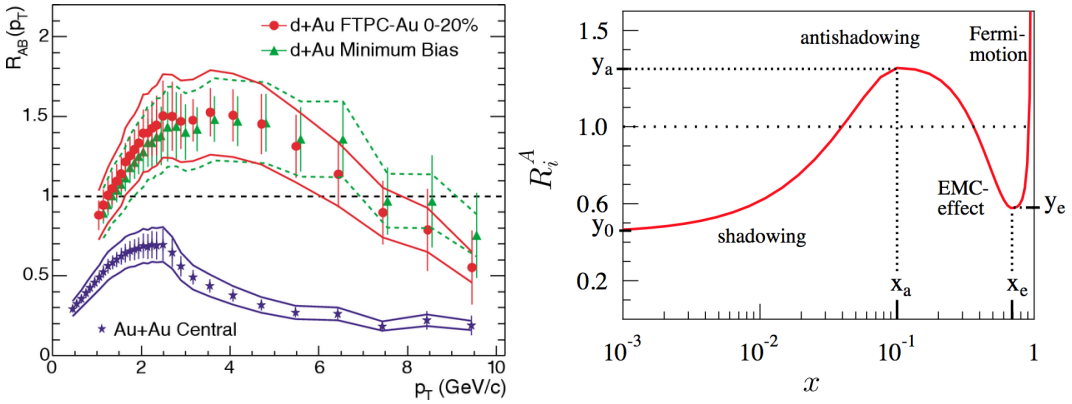

FIGURE 1.10: Left: R_{AA} of charged hadrons, measured in d–Au and central Au–Au collisions at $\sqrt{s_{\mathrm{NN}}}$ =200 GeV, by STAR[53]. Right: $R_i^A(x)$ as a function of Bjorken scaling variable x for a given fixed Q^2. $R_i^A(x)$ is the variable commonly used to study nuclear modification effects. $R_i^A(x)$ is defined as the nuclear structure function $F_2^A(x, Q^2)$ of nucleus A divided by the nucleon structure function for a free nucleon and normalized to the mass number of the nucleus A[60].

This approach predicts that the nuclei accelerated to near the speed of light, at RHIC and at the LHC, would reach an upper limit of gluon concentration that can be described in the framework of the Color Glass Condensate (CGC) models[61, 62]. In this framework the initial conditions in p–A collisions are created by a hit of the projectile proton with a bunch of nucleons (a dense field of gluon) simultaneously instead of individual nucleon-nucleon interactions, making it harder for particles with a given momentum to be produced. The measurement of identified particle spectra in p–Pb and pp collisions provides the reference for Pb–Pb collisions and is also helpful to understand the initial CNM effects. Furthermore, the Bjorken scaling variable x at the LHC can reach values about two orders of magnitude smaller than at RHIC. Thus, p–Pb collisions at the LHC allow for investigation of fundamental properties of QCD at very low fractional parton momentum x and very high density regime, where parton shadowing and novel phenomena like saturation, e.g. as implemented in CGC model, may appear[62].

1.4 Photon probe

Photon detection is one of the most promising methods to characterize the medium created at the earliest phase of the collision and its phase of expansion. In this chapter, the processes for photon production are introduced briefly. The motivation to study neutral mesons will also be highlighted. Then one of electromagnetic calorimeters in ALICE with PHOS used to measure photons is presented.

1.4.1 Photon production

As an electromagnetic particle, photon does not undergo strong interaction with the hot and dense medium produced in hadron-hadron or A–A collisions. Also its mean free path is larger than the typical size of collision system ($\sim$ 10 fm). Thus photon can carry the initial information once they were created during the collision evolution at different stages (pre-equilibrium, thermal QGP, hot hadron gas and hadronic decay)[63]. Depending on their origin, photons are classified into categories as below:

- **Prompt photons** are produced in early stage of collisions in hard or pre- equilibrium partonic cascade processes, Compton scattering ($q(\bar{q}) + g \rightarrow \gamma + q(\bar{q})$), annihilation ($q + \bar{q} \rightarrow \gamma + g$) from the two incoming partons and quark fragmentation ($q(\bar{q}) \rightarrow q(\bar{q}) + \gamma$). The production rate can be calculated through perturbative QCD. Among these processes, Compton scattering is dominant in the leading order calculations. While in next-to-leading order calculation, more complicated processes contribute to the total photon cross section[64]:

$$\frac{d^2\sigma}{d\vec{p}_T d\eta} = \frac{d^2\sigma^{(D)}}{d\vec{p}_T d\eta} + \frac{d^2\sigma^{(F)}}{d\vec{p}_T d\eta} \tag{1.10}$$

  ,where D denotes the contribution from Compton scattering and annihilation and F stands for the fragmentation photons. The two terms can be expressed explicitly as[65]

$$\begin{aligned}\frac{d^2\sigma^{(D)}}{d\vec{p}_T d\eta} = \sum_{i,j=q,\bar{q},g} \int dx_1 dx_2 F_{i/h_1(x_1,M)} F_{j/h_2}(x_j, M) \frac{\alpha_s \mu_R}{2\pi} \\ \times \left(\frac{d^2\hat{\sigma}_{ij}}{d\vec{p}_T d\eta} + \frac{\alpha_s(\mu_R)}{2\pi} K_{ij}^{(D)}(\mu_R, M, M_F) \right)\end{aligned} \tag{1.11}$$

and

$$\frac{d\sigma^{(F)}}{d\vec{p}_T d\eta} = \sum_{i,j,k=q,\bar{q},g} \int dx_1 dx_2 \frac{dz}{z^2} F_{i/h_1(x_1,M)} F_{j/h_2}(x_j, M) D_{\gamma/k}(z, M_F) \times \frac{\alpha_s \mu_R}{2\pi} \Big(\frac{d\hat{\sigma}^k_{ij}}{d\vec{p}_T d\eta} + \frac{\alpha_s(\mu_R)}{2\pi} K^{(F)}_{ij,k}(\mu_R, M, M_F) \Big) \tag{1.12}$$

, where F is the parton distribution function, D is the fragmentation function and $\alpha_s(\mu_R)$ is the strong coupling constant which depends on the normalization scale μ_R. Figure 1.11a presents the world wide inclusive and isolated direct photon production cross sections compared with JETPHOX[66] NLO calculations using CTEQ6M[67] fragmentation function. A good agreement over 9 orders of magnitude in cross sections between the data and theory is observed. Figure 1.11b presents the ratio of data/theory as a function of $x_T = 2p_T/\sqrt{s}$. It exhibits a promising agreement between theory and data in the whole x_T range with the exception of the E706 data.

- **Thermal photons** , which are produced during the QGP thermalization [68–71] phase. The radiation rate of photon with energy E and momentum p is related to the imaginary part of photon self-energy:

$$E\frac{dR}{d^3p} = \frac{-2}{(2\pi)^3} Im \prod_{\mu}^{R,\mu} \frac{1}{e^{E/T} - 1} \tag{1.13}$$

, where $\prod_{\mu}^{R,\mu}$ is the self-energy under finite temperature T. Using the relativistic theory formulation and considering the infrared contribution[72, 73], the final results can be written as:

$$E\frac{dR}{d^3p} = \frac{5}{9}\frac{\alpha\alpha_s}{2\pi} T^2 e^{-E/T} ln(\frac{2.912}{g^2}\frac{E}{T}). \tag{1.14}$$

We could note that production rate exhibits a $e^{-E_\gamma/T}$ behavior at low p_T. The thermal photon spectra is important to probe the hot and dense system temperature. However, it is a great challenge to measure it experimentally since the background is huge and this leads to a strong theoretical dependence.

- **Jet-photon conversion** [74], produced in secondary interactions of hard parton jets with thermal partons in QGP. The dominant processes are jet-photon conversion ($q_{hard} + \bar{q} \rightarrow \gamma + g$ and $q_{hard} + g_{\mathrm{QGP}} \rightarrow \gamma + g$) and medium introduced photon

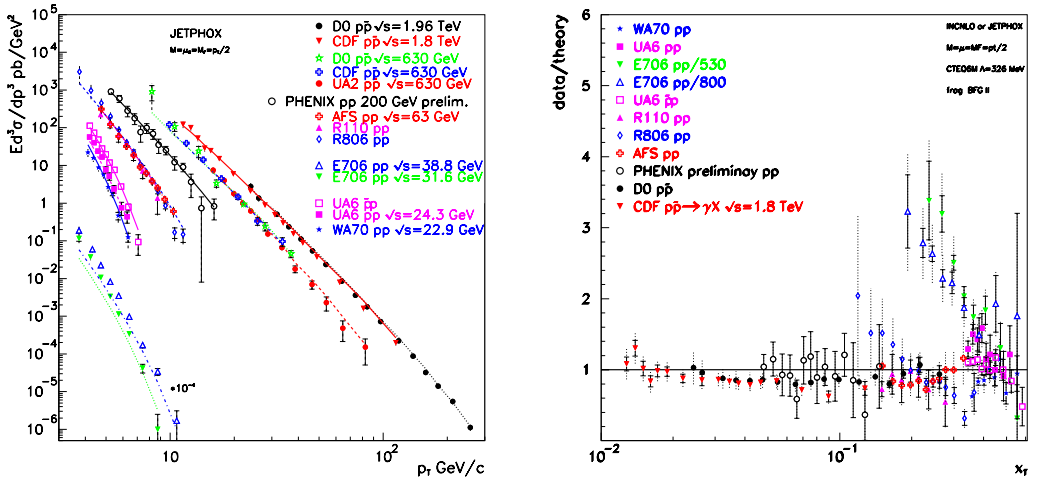

(A) Prompt photons and QGP thermal radiation

(B) Fragmentation photons

FIGURE 1.11: World-wide inclusive and isolated direct photon cross section (a) and data/theory as a function of $x_T = 2p_T/\sqrt{s}$. (b) in pp and p$\bar{\text{p}}$ compared to JETPHOX NLO with CTEQ6M and $M = \mu_R = M_F = \frac{1}{2}p_T$[65].

bremsstrahlung. Its contribution can be expressed as:

$$E_\gamma \frac{dN_\gamma^{(anni)}}{d^3p_\gamma d^4x} = E_\gamma \frac{dN_\gamma^{(com)}}{d^3p_\gamma d^4x} = \frac{\alpha\alpha_s}{8\pi^2}\sum_{f=1}^{N_f}(\frac{e_q f}{e})^2[f_q(\mathbf{p}_\gamma) + f_{\bar{q}}(\mathbf{p}_\gamma)]T^2 \times [ln(\frac{4E_\gamma T}{m^2}) - 1.916]. \tag{1.15}$$

If we include the u, d and s quark flavors, $\sum_f = e_{q_f}^2/e^2 = 2/3$. Also here we introduce mass m to shield the infrared divergence. This calculations are well developed to correct the parton energy loss[75].

- **Photons form hot hadron gas.** The hot hadron gas is produced after the freeze-out of quark-gluon plasma. The photons are produced because of the hadronic reactions. The spectrum of these photons dominates at lower $p_{\mathrm{T}}(< 1$ GeV/c). The calculation was performed by Kapusta et al.[71].

- **Decay photons** are the decay products of hadronic resonances. The decay photons from π^0, η, ω etc. are the main contribution (90% more) to the final inclusive photons. Thus experimentally, to extract the direct photon spectra it is crucial to reconstruct the neutral mesons spectra for the background subtraction. In experiment, depending on the detector granularity and the π^0 momentum range, three methods of invariant mass analysis, shower shape analysis and track matching method will be used, more detailed strategies can be found in Chapter 3.

As for the direct photons[43, 68], literally, it means that photons emerged from the collisions directly. Henceforward, so called "direct photon" includes prompt photons, thermal photons and fragmentation photons except for decay photons. From the view of experiment, we can extract direct photon spectrum by subtracting decay photons from inclusive photon spectra. Detailed split of direct photons components is strongly dependent on models.

1.4.2 Role of π^0 measurement

In this thesis, we focus on the π^0 measurement with ALICE PHOS. The measurement is top priority for electromagnetic calorimeters. They will play an IMPORTANT role at initial stage of data taking and lead an important role on jet and flow physics. The neutral pions with their photon decays will be studied in this thesis. The role of π^0 measurement will be emphasized.

- **Calibration of the EM-calorimeters**

  From the final observed hadrons in pp and A–A collisions, about one third are neutral pions. π^0 with a nominal mass of 135 MeV/c^2 has a 98% branching ratio to 2γ. We can then reconstruct them by 2γ invariant mass analysis to calibrate the electromagnetic calorimeters in an absolute or relative way, especially at early stage of real data analysis in order to understand the detector.

- **Test of pQCD**

  The pQCD describes the particle production cross section at large transverse momentum well by considering the factorization holds:

$$\frac{d\sigma^{AB\to C}}{dp_T dy} = \sum_{a,b,c} \int dx_a dx_b \frac{dz}{z^2} F_{a/A}(x_a, M) F_{b/B}(x_b, M) \times D_{C/c}(z, M_F) \frac{d\hat{\sigma}^{ab\to c}}{dp_{T,c} dy_c}(\mu, M, M_F) \tag{1.16}$$

  , where F is the parton density function, $D_{C/c}$ is the fragmentation function from the parton c to a hadron C, and $\hat{\sigma}^{ab\to c}$ is the hard cross section between the partons a and b from A and B respectively to produce a parton c [96-99]. In practice, the next-to-leading order approximation is used to calculate these functions. However, there remain unphysical renormalization factors μ, fragmentation scale M_F and factorization factor M which are adjustable.

- **Scaling behavior**

  The scaling behavior have been found by comparison of the world-wide data from

SIS energy to RHIC energy. The implement of LHC data points allow us extend to small x_T range and to explore the system thermal properties by theoretical fit procedure.

- **High p_{T} π^0 spectra for nuclear matter effects**

  As shown in Section 1.3 on the nuclear modification factor, the suppression at high p_{T} in p–Pb collisions at RHIC is observed for all the neutral mesons. To disentangle the hot and cold nuclear matter effects, p–Pb collisions is introduced (Section 1.3.2). ALICE has the capability to measure them up to higher p_{T}, which allow to better understand if pQCD holds, and to study the CNM effects at extreme high momentum up to 50 GeV/c. In this analysis, the neutral pion spectrum in p–Pb at 5.02 TeV are analyzed.

Chapter 2

Experimental Setup

This chapter will give an overview of the experimental setup used for in this analysis. The first section is a brief introduction to the Large Hadron Collider (LHC) accelerator complex. Then, the main features of the ALICE detector layout will be presented. Lastly, a detailed description of PHOton Spectrometer (PHOS) will be given.

2.1 Large Hadron Collider

The Large Hadron Collider (LHC)[1] is a collider facility designed to deliver collisions of protons and nuclei. The maximal dipole magnetic filed of 8.33 Tesla allows for energies up to 7 TeV for protons and 2.76 TeV per nucleon for lead ions (14 TeV and 5.5 TeV in colliding system center of mass respectively). The two-in-one magnet design of the LHC does not allow for different energies of the clockwise and counter-clockwise beams. Center of mass of the non-symmetric colliding system moves in the laboratory frame in direction of the more energetic beam. Luminosity is expected to rise up to $10^{34}\ cm^{-2}s^{-1}$ for pp and $10^{27}\ cm^{-2}s^{-1}$ for the Pb–Pb running. Up to the point of writing of this thesis, the LHC delivered collisions at center of mass of $\sqrt{s}$ = 900 GeV, 2.76 TeV, 7 and 8 TeV for pp, $\sqrt{s_{\mathrm{NN}}}$ = 2.76 TeV for Pb–Pb and $\sqrt{s_{\mathrm{NN}}}$ = 5.02 TeV for p–Pb (in both directions). The luminosities delivered are shown on Figure 2.1.

The LHC is the latest stage of the accelerator complex at CERN (Figure 2.2). Circumference of the LHC is 27 km, the ring is 50 to 170 meters under ground. It is composed of 1232 dipole and 392 quadrupole magnets with superconducting coils, cooled down to 1.7 K. The radio-frequency (RF) acceleration and injection system operates at 400 MHz frequency (decrease to 200 MHz is foreseen), the main LHC operating frequency is 40 MHz (25 ns bunches). Single bucket (RF slot) out of 10 is filled with a bunch. Out of

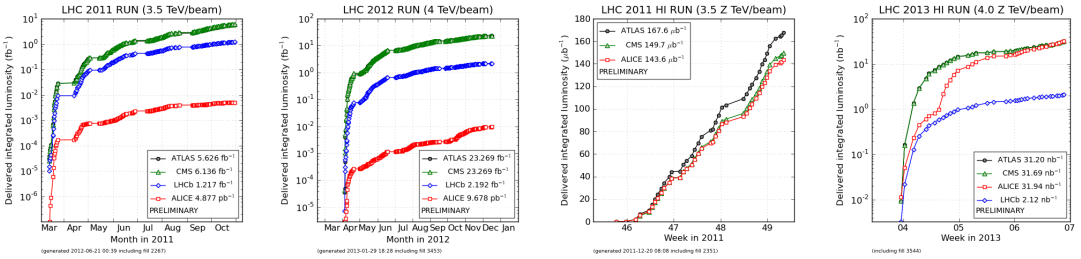

(A) pp of 7 TeV (B) pp of 8 TeV (C) Pb–Pb of 2.76 TeV (D) p–Pb of 5.02 TeV

FIGURE 2.1: The luminosities delivered by the LHC to the four experiments.

3564 possible bunches in the ring, maximum of 2808 are filled. The energy stored in the beam is up to 362 MJ, additionally there are about 600 MJ stored in the magnets.

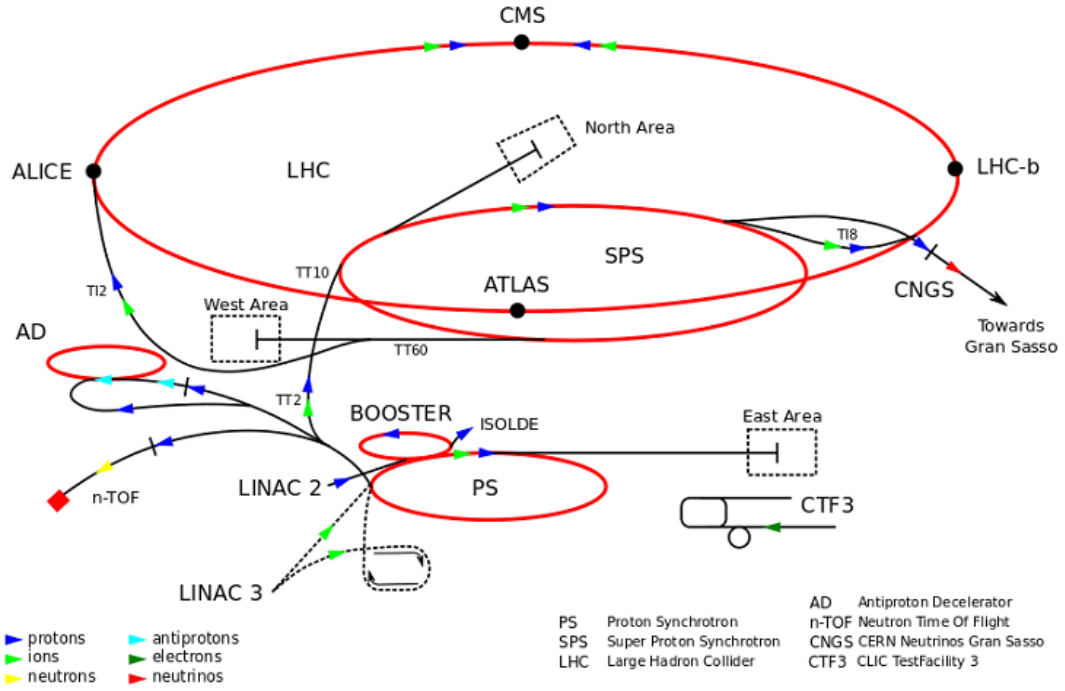

FIGURE 2.2: Map of the CERN accelerator complex

The operating cycle for one fill of the LHC can be extended to about 10 hours, thanks to ultra high beam vacuum of about 10^{-10} Torr (equivalent of outer space vacuum at around 1000 km above Earth surface) and to the system of horizontally and vertically focusing quadrupoles. The quadrupoles provide strong focusing[76] of the beam to correct for different angular momenta of the protons in the bunches. A proper series of vertically and horizontally focusing (defocussing in transverse direction) magnets leads to overall beam focusing. The magnets focusing in a given plane are placed at positions, where the deviation from circular orbit is large in the focusing plane, but small in the defocussing plane. The sequence of magnets is optimized to provide minimal betatron oscillation amplitude (β) at the interaction points (narrow distribution in the transverse plain).

The longitudinal profile of the bunch is focused by the property of the RF cavity, which gives higher momentum kick to particles arriving later (the lower momentum ones). The particles escaping the focusing ability of the RF system are still kept oscillating around synchronous position (synchrotron oscillation). This is due to interplay of velocity and orbit length in constant magnetic field. The quadrupole setting define energy threshold, below which the orbit time decreases with increasing momentum and above which the orbit time increases with increasing momentum.

The filling of the LHC requires 12 SPS cycles of 21.6 s. Though due to injection of pilot bunches, recalibration of the machine based on the pilots, ramping the beam and magnets, the theoretical minimum of the LHC turnaround is close to 60 minutes. The turnaround is several hours in the real life operation.

The ring is subdivided into 8 octants (Figure 2.3), each bearing one experimental cavern or beam facility. There are four major experiments located on the LHC ring and several smaller ones. Two multi purpose experiments ATLAS[77] and CMS[78] are targeting mainly the particle physics of the standard model and search for hints beyond the model. The LHCb[79] experiment specializes in study of b quark physics and CP symmetry violation. The ALICE[5] experiment targets the physics of heavy ion collisions.

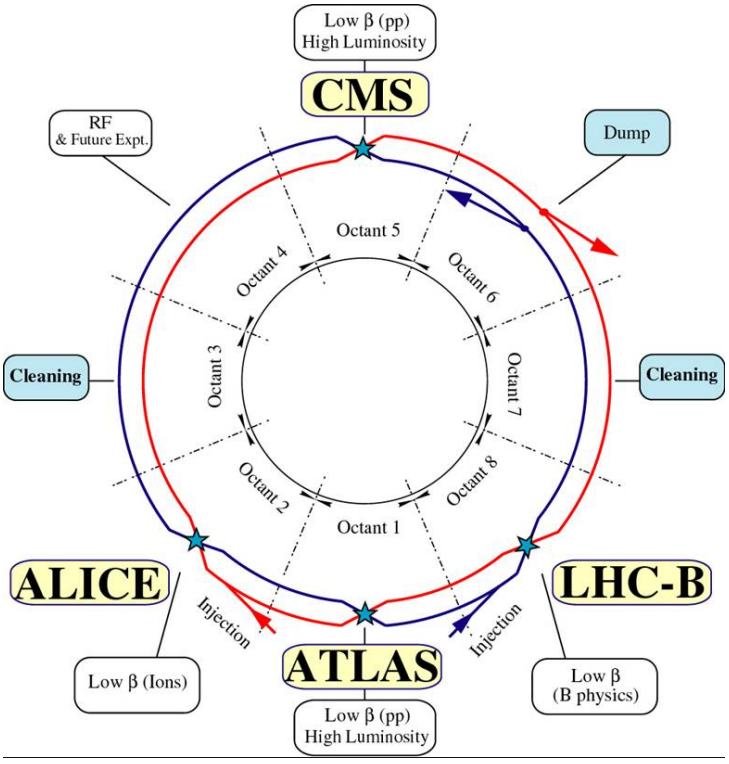

FIGURE 2.3: LHC schematics with division to the octants.

2.2 A Large Ion Collider Experiment

A Large Ion Collider Experiment (ALICE) scientific program concentrates on study of the strongly interacting hot and dense medium that arises in the heavy ion collisions. For this purpose, ALICE design is optimized for high multiplicity environments of the heavy ion collisions and has powerful particle identification capabilities.

ALICE (Figure 2.4) central barrel is fully enclosed in 0.5 Tesla solenoid magnet and it's combined tracking covers at least $|\eta| < 0.9$ units of pseudo-rapidity. There is a forward muon spectrometer[80] outside of the magnet with coverage of $-4 < \eta < -2.5$ and equipped with 0.2 Tesla dipole magnet.

The core of ALICE are tracking detectors ordered in the central barrel. The main tracking performance is delivered by the gas filled Time Projection Chamber (TPC)[81, 82] of 88 m^3 with outer radius of 250 cm. There are six layers of silicon based Inner Tracking System (ITS)[83] closer to beam pipe in the barrel. The ITS increases precision for the tracking, especially for low energetic particles, enhances primary and secondary vertexes resolution and provides PID for low energetic particles.

There are two layers of PID detectors outside the TPC; Transition Radiation Detector (TRD)[84] and Time of Flight detector (TOF)[85], additionally there is a partial coverage of High Momentum Particle Identification (HMPID)[86].

Array of forward detectors[87] provide basic collision triggering and centrality measurements (V0), precise collision time and vertex position (T0), forward multiplicity (FMD), impact parameter (ZDC) and forward photon multiplicity (PMD) measurements.

Electromagnetic calorimetry in ALICE is supported by three detectors with partial coverage; Electromagnetic Calorimeter (EMCal)[88], PHOS[89] and DCal [90].

2.2.1 Tracking detectors

Tracking of the charged particles is performed by the TPC and ITS. The TPC is a large drift chamber filled with mixture of neon, carbon dioxide and nitrogen gases. The drift volume is separated into 18 sectors in the azimuth, each having inner and outer readout chamber. The readout is carried out by multi-wire proportional chambers with cathode pad readout. Longitudinally the TPC is separated into two regions each with drift field oriented towards end cap of the detector, separated by the central 100 kV electrode (400 Vcm drift field). Due to the drift time of approx. 88 μs, the event rate of TPC is limited and it is susceptible to pileup events.

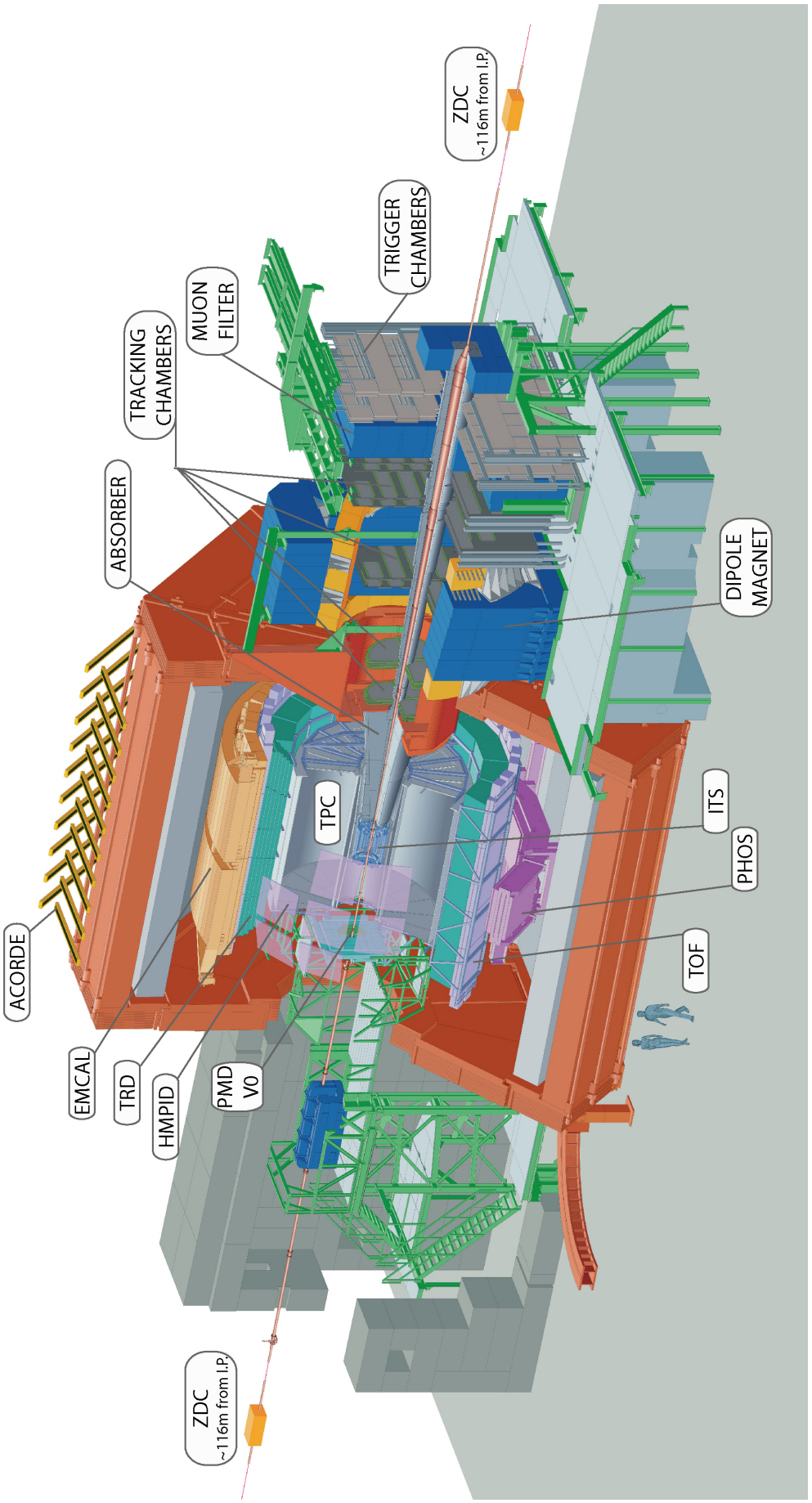

FIGURE 2.4: ALICE detectors schematic layout at LHC.

The ITS is composed of six silicon layers of three different detector technologies. The innermost two layers are populated with high granularity Silicon Pixel Detectors (SPD), middle layers with Silicon Drift Detectors (SDD) and outer layers with Silicon Strip Detectors (SSD). The four outer layers feature analog readout and are therefore capable of dE/dx measurements. Spatial resolutions of the silicon technologies are 12×100, 35×25 and 20×830 μm respectively ($r\phi \times z$, where z is along beam axis). Allowing for impact parameter resolution of around 70 μm in $r\phi$.

The performance of TPC and ITS tracking allows to track particles of transverse momenta (p_{T}) up to 100 GeV/c with less than 20% resolution on the momentum and down to 0.1 GeV/c with resolution around 3% (Figure 2.5) and provides impact parameter resolution and vertex resolutions shown on Figure 2.6. The ITS vertex resolution is also good enough to allow for detection of decays of single charmed mesons down to approximately $p_{\mathrm{T}} = 2$ GeV/c.

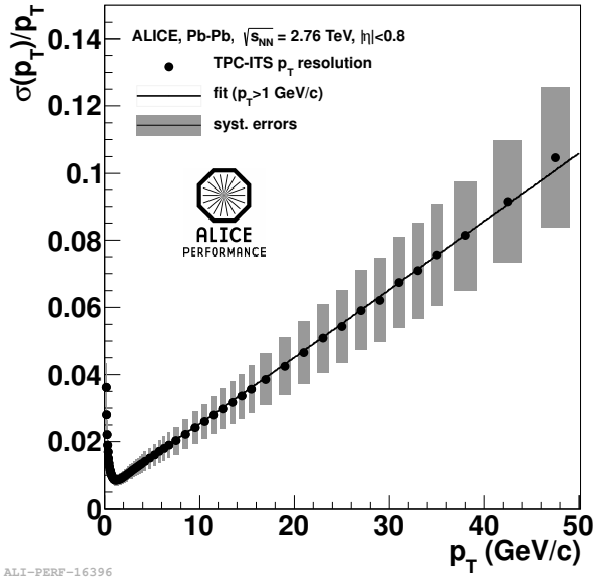

FIGURE 2.5: Track momentum resolution as a function of p_{T} of combined ITS and TPC tracking.

2.2.2 PID detectors

As already mentioned, the tracking detectors are also capable of particle identification(PID) through the $\mathrm{d}E/\mathrm{d}x$ method. ITS can provide $\mathrm{d}E/\mathrm{d}x$ for very low momentum particles below approx. $p_{\mathrm{T}} = 0.2$ GeV/c, TPC for particles below approx. $p_{\mathrm{T}} = 1$ GeV/c (Figure 2.7)[91, 92].

The TRD[84] acts primarily as a pion rejection for particle momenta above the TPC electron/pion distinction ability (p_{T} >1 GeV/c). Transition radiation photons coming

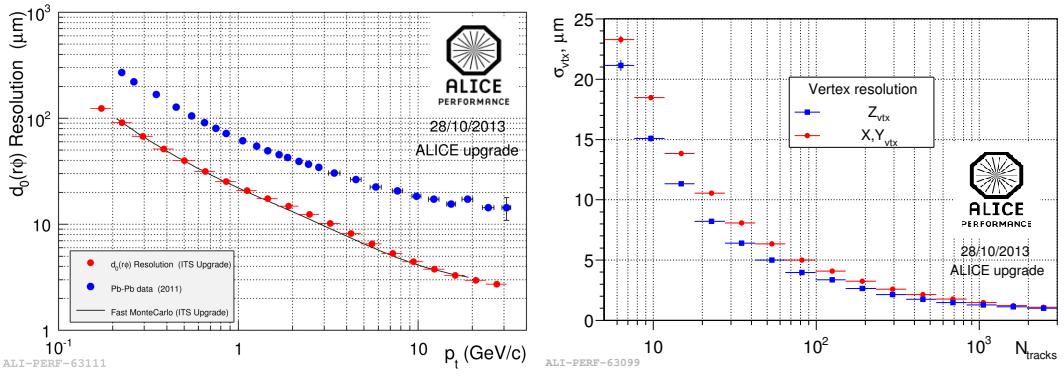

FIGURE 2.6: Left: ITS transverse impact parameter resolution in Pb–Pb, data and MC. Right: Vertex resolution in Pb–Pb collisions at $\sqrt{s_{\mathrm{NN}}} = 2.76$ TeV as a function of half of the tracklets multiplicity of the event.

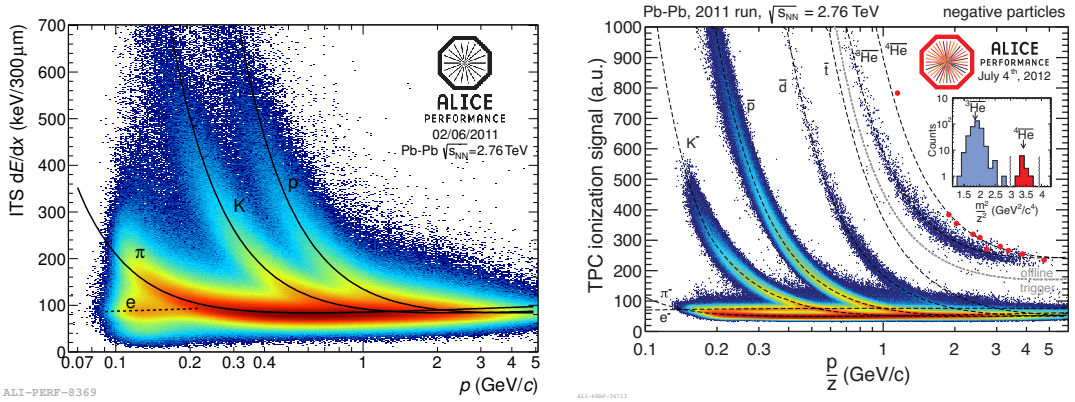

FIGURE 2.7: Left: ITS $\mathrm{d}E/\mathrm{d}x$ PID versus particle p_{T}. Right: TPC $\mathrm{d}E/\mathrm{d}x$ PID versus particle p_{T} [93].

from particles passing through boundary of two media with different refraction indexes are exploited. The TRD is composed of polypropylene radiator, xenon and carbon dioxide filled drift region and multi wire proportional chamber readout. The TRD way of operation is shown on Figure 2.8. The detector is located right after TPC and is composed of 6 layers of modules. The provided electron/pion rejection is in order of 100.

The TOF detector[85] is an array of fast Multi-gap Resistive Plate Chambers, with time resolution in order of 50 ps. The purpose of the TOF is to provide a time of flight PID for charged particles up to $\sim p_{\mathrm{T}} = 4$ GeV/c (Figure 3.6).

The HMPID[86] is a detector with partial central barrel coverage (about 5%). It uses Cherenkov radiation to extend the PID of charged particles above the PID capabilities of the other central barrel detectors. The detector is composed of C_6F_{14} UV transparent Cherenkov radiator, followed by multi-wire proportional chamber. The gap in between radiator and MWPC is filled with methane and any electrons generated inside are collected by positively charged electrode to prevent them from entering the MWPC

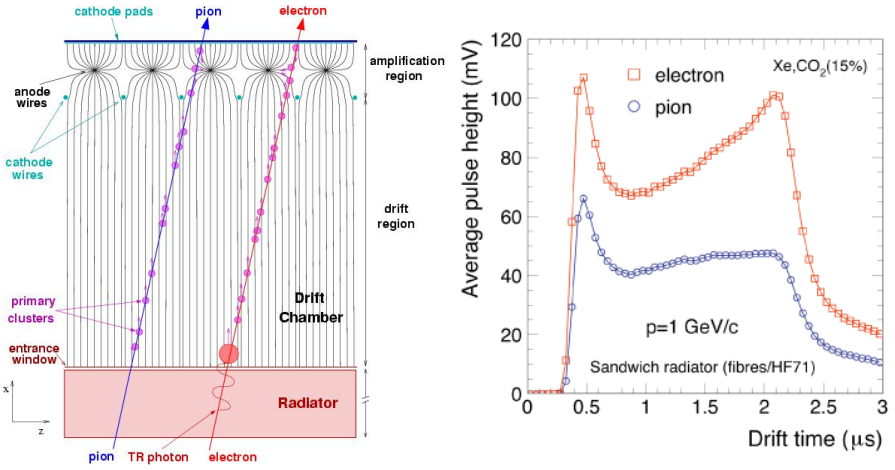

FIGURE 2.8: Left: TRD module function principle. Right: TRD signal shape as a function of time[84].

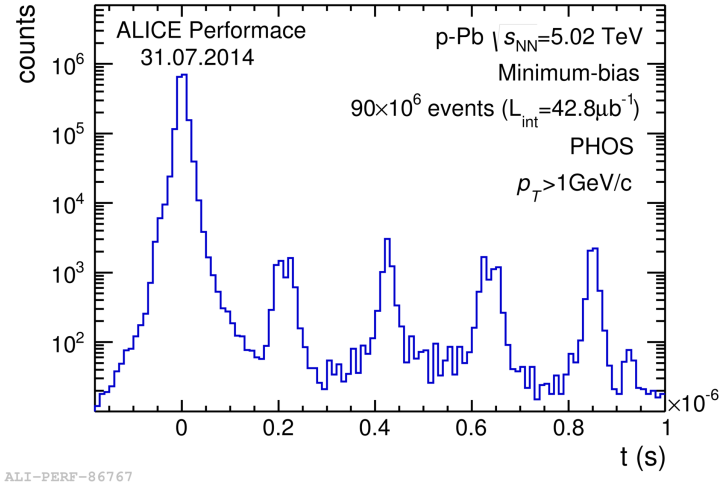

FIGURE 2.9: TOF $\beta - p$ performance in Pb–Pb run 2011.

sensitive volume. The Cherenkov photons and ionization electrons are read out by CsI coated pad cathode of the MWPC. PID performance of the HMPID is shown on Figure 2.10. With the HMPID it is possible to differentiate pions from kaons up to ~ 3 GeV/c and kaons from protons up to ~ 5 GeV/c.

2.2.3 EM-Calorimetry

The ALICE EMCal detector[88] is a sampling calorimeter of shashlik design and consists of 10 full size super-modules (SM) that cover the pseudo-rapidity range $|\eta| < 0.7$ and 100° in azimuth and two additional 1/3 size SMs, which increase the coverage in azimuth by 6.6°. One SM consists of 1152 towers, each with individual avalanche photodiode readout. The tower dimensions are $6 \times 6 \times 24.6$ cm^3 with an average Moliere radius of 3.20 cm. The DCal is technologically identical to EMCal. The DCal coverage spans

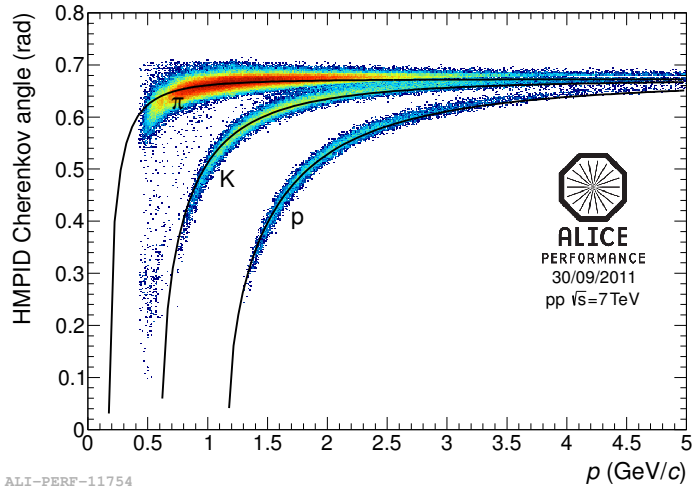

FIGURE 2.10: HMPID particle identification performance[93].

over 67° in azimuth, but only 2/3 coverage in pseudo-rapidity in respect to EMCal super modules, as the mid rapidity region is occupied by the PHOS. In between PHOS and DCal active volumes, there is a gap of $10cm$. DCal is fully back-to-back with EMCal.

The PHOS[89] is a calorimeter with higher granularity (Figure 2.11) than EMCal (tower size of $2.2 \times 2.2 \times 18\ cm^3$), lead glass scintillator and identical readout to EMCal. The whole PHOS is kept at $-25°C$ to increase the light yield of the scintillator crystal by factor of 3 in respect to room temperature. PHOS covers 100° in azimuth and $\eta < 0.12$. It is fully back-to-back with EMCal. The PHOS will be discussed in much more detail in the following Section 2.3.

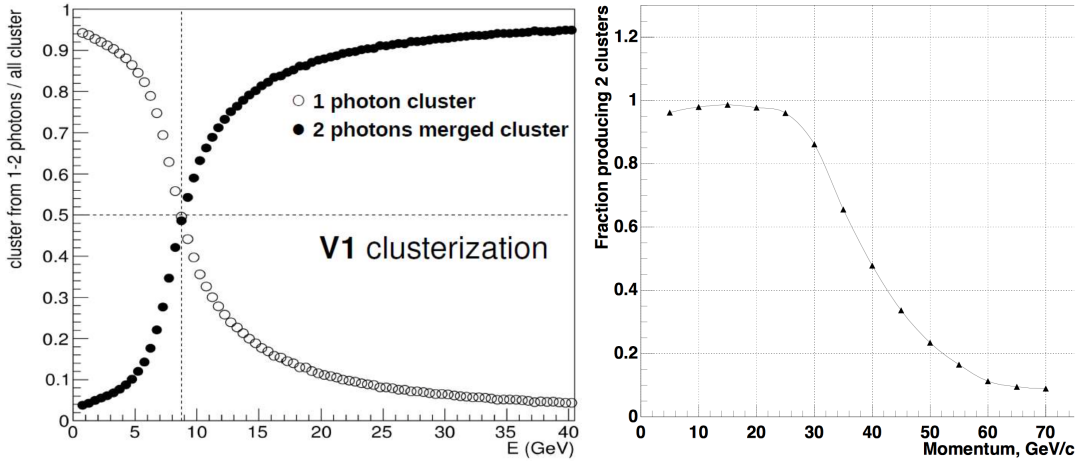

FIGURE 2.11: Two π^0 decay photon separation. Left for EMCal, right for PHOS.

2.2.4 Forward detectors

The V0 detector consists of 2 arrays of scintillators. Each interaction point side (AC) of the array is located at different distance from the interaction point (same for T0 and FMD), due to presence of the muon arm on C side (Figure 2.12). On top of the basic L0 interaction trigger and centrality triggers, the V0 also provides background rejection for the muon arm and centrality signal to other detectors trigger systems (EMCal, DCal, PHOS).

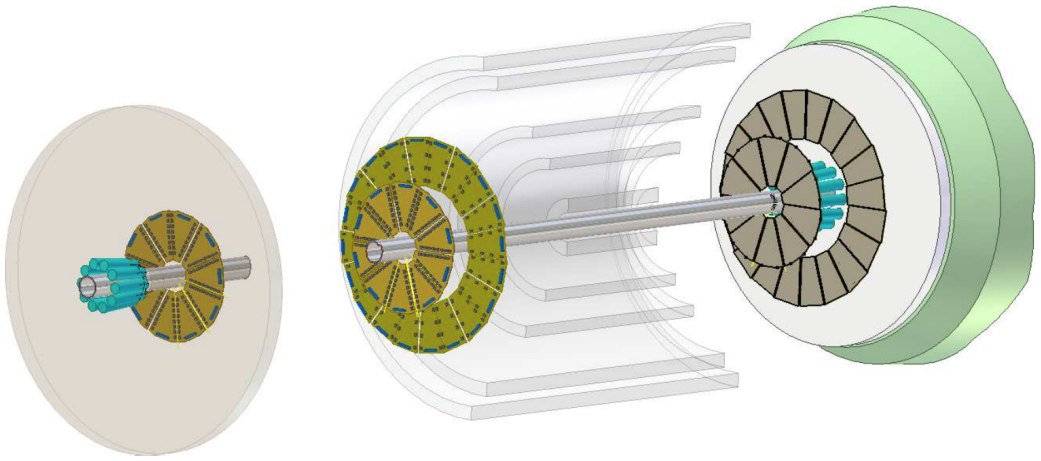

FIGURE 2.12: Schematic of the placement of T0, V0 and FMD on both sides of the interaction point of ALICE. The five layers of ITS are sketched in the central region.

The T0 detector in difference to V0 consists of 2 arrays of photo-multiplier tubes equipped with Cherenkov radiators. It is capable of locating the primary vertex with 1.5 cm precision. T0 can also act as redundancy for the V0. The FMD is composed of silicon strip detectors and its main target is to extend the ITS charged particle multiplicity measurements to pseudo-rapidity range $-3.4 < \eta < 5$. There are small overlaps of the regions of FMD and ITS plates.

The ZDC is a set of calorimeters, located rather far (116 m) on both sides of the interaction point. Each set of calorimeters consists of one proton and one neutron calorimeter, located at zero degree angle to the beam (neutrons in between the two beam pipes, protons next to beam pipe to compensate for p trajectory shift by ALICE magnetic fields).

Additionally there are two electromagnetic calorimeters placed at 7 m from the interaction point. The main purpose of the ZDC is to detect spectator nucleons of the collisions. It can provide luminosity, centrality and reaction plane measurements.

The forward muon spectrometer covers pseudo-rapidity one forward range of $-4 < \eta < -2.5$. It composes of high granularity (100 μm spacial resolution) tracking cathode pad

chambers stacked in 10 levels (5 stations). There is a forward absorber made of carbon and concrete to absorb other particles coming from the collision in front of the tracking chambers. Additionally to protect from high rapidity particle background, there is beam shield of tungsten, lead a steel. Muon filter wall is located behind the tracking plates and separates the later 4 levels (2 stations) of muon trigger made of resistive plate chambers. Dipole magnet of 0.2 Tesla is placed in between the tracking strips to bend the trajectory of the muons.

The physics program of the muon spectrometer concentrates on measurements of di-muon decay channels of the heavy quarkonia and heavy flavor measurements through the open charm and beauty.

2.2.5 ALICE trigger and data acquisition

The ALICE Central Trigger Processor (CTP) collects the trigger signals from the detectors. It selects events with various options and rates and allows to perform a down-scaling of these rates in order to fit the bandwidth requirements of the acquisition system. In order to selectreject an event as fast as possible the triggers form 3 groups of the trigger levels depending on their response time:

- **L0 (Level-0)** : these trigger signals arrive to the CTP first. They are sent by the fastest detectors, such as the SPD, V0, T0 and the muon trigger system. In order to select a certain class of events, a logic AND and OR is used when combining these signals in the CTP.
- **L1 (Level-1)** : these trigger signals are sent from slower detectors and must be delivered to the detectors in $6.5\mu s$ after the collision took place.
- **L2 (Level-2)** : the last trigger level. The time of arrival of $\sim$ 100 μs after the collision is constrained by the TPC drift time and by the past-future protection circuit. The latter looks for other events of a certain type in time windows before and after the considered collision, thus helping the rejection of the pile-up events and the read out of the detectors.

The ALICE Data AcQuisition (DAQ) system copes with both pp collisions with high rates and relatively small event sizes, on the one hand, and with Pb–Pb collisions with lower rates but larger event sizes (up to 1.25 GBs sent to the storage elements), on the other hand. After the CTP selects an event, the trigger signal is sent to the FERO (Front-End Read-Out) electronics of the involved detectors. The data are then transmitted to the computer farms LDCs (Local Data Concentrator) which build the event fragments

from the front-end electronics into sub-events. Those sub-events are then transferred to the GDC (Global Data Collectors) which build the whole event combining all the sub-events from various LDCs. The whole event is then sent by the GDC to the storage facilities.

2.3 PHOton Spectrometer

PHOton Spectrometer (PHOS) was designed to measure π^0, direct photons and study of γ-jethadrons correlations over a large momentum range to probe the properties of QCD matter. It is also expected to measure the soft photon down to 0.3 GeV to explore the dynamics of the thermal medium.

PHOS is a high resolution electro-magnetic calorimeter placed at a radial distance of 460 cm from the interaction point. PHOS covers 100^o in azimuth and 0.24 units in pseudo-rapidity ($|\eta| < 0.12$).

PHOS consists of two detectors, an electromagnetic calorimeter (EMC) and a Charged ParticleVeto(CPV) detector. The calorimeter consists of lead tungstate crystals ($PbWO_4$) with a high granularity and high energy resolution which are read out by APDs (Avalanche Photon Diode). The CPV consist of multi-wire proportional chambers with one CPV module for each EMC module. The CPV will provide discrimination against charged particles. Due to CPV not installed at LHC Run I (one of the CPV module is ready and installed for LHC Run II), the EMC is the main focus in this section.

2.3.1 Physical layout

PHOS consists in 5 identical modules, as shown in Figure 2.13a with the yellow color. Each module consists in a matrix of 56×64 $PbWO_4$ crystals. The $PbWO_4$[94] is a fast scintillation crystal (high intrinsic time resolution of 0.13 ns) with a light emission of 400 nm to 500 nm. Each crystal has a dimension of $22 \times 22 \times 180$ mm^3. The length (180 mm) corresponds to a $20X_0$ radiation length to fully contain high energy electromagnetic shower particles. It provides a fine granularity of $\Delta\phi \times \Delta\eta = 4.8 \cdot 10^{-3} \times 4.3 \cdot 10^{-3}$ to separate the different electromagnetic showers. The sketch of the PHOS assembly is illustrated in Figure 2.13.

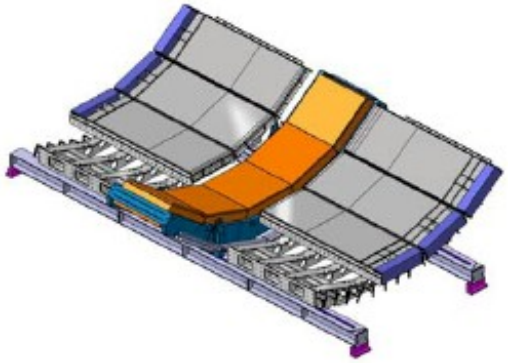

(A) PHOS layout

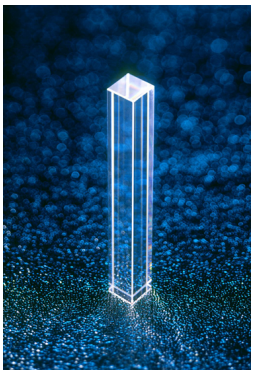

(B) $PbWO_4$ crystal

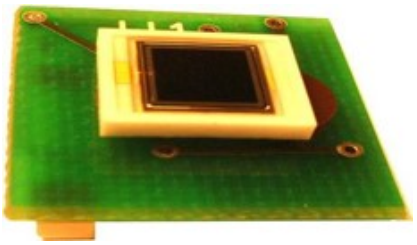

(C) APD

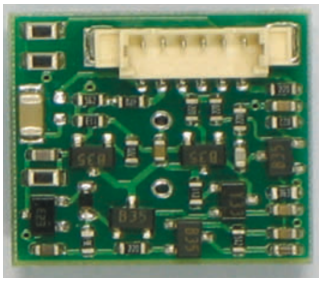

(D) CSP

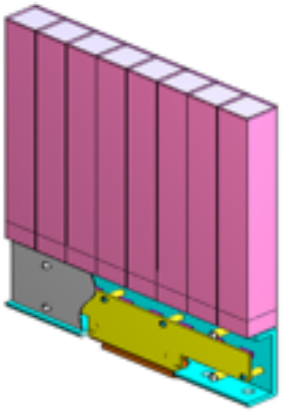

(E) Strip unit

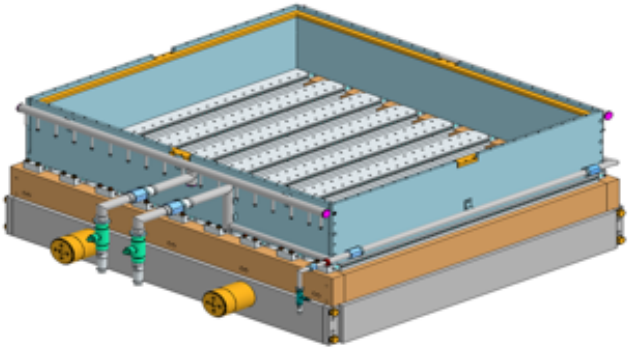

(F) PHOS module

FIGURE 2.13: ALICE PHOS detector and the components of $PbWO_4$ crystal, APD, CSP, strip unit and a PHOS module.

2.3.2 Signal collection

The photon signal is collected by APDs with an active area of $5 \times 5\ mm^3$. They are mounted at the bottom of the $PbWO_4$ crystal and protected by a thin epoxy shield on the top of surface. The typical spectra response is about 600 nm with a quantum efficiency around 85%. The APD gain factor increases with a decreasing temperature to a factor 3 at -25^{o}C compared to the gain at room temperature with a bias voltage of 350 V and an input capacitance of 80 pF .

The low noise Charged Sensitive Preamplifier (CSP) are mounted at the back side of

APDs to detect the scintillation light and collect the analog signals. The power supply is ranged from +12 to 6 V with a power consumption of 64 mW. The gain of CSP is measured to be 0.78 $V \cdot pC^{-1}$ with a RMS noise of 200–500 electrons.

Each 8×2 crystals are assembled into a crystal strip unit and two strip units are connected to a FEE (Front-End Electronics)[95, 96]. The FEEs are developed and manufactured by ALICE Wuhan-China group to process the electronic signal from CSP. To fit the requirement of ALICE, two 10-bit 10 MHz sampling ADCs are used for two different dynamics ranges from 5 MeV to 5 GeV for high gain channels and 80 MeV to 80 GeV for low gain channels. In addition, FEEs also provide fast 2×2 analog energy sum outputs to TRUs (Trigger Region Unit) for a L0L1 trigger decision generation. Each FEE has 32 detection readouts with dual gains.

For each module, in total, there are one hundred twelve FEEs, eight Trigger Readout Unit (TRU) and four Readout Control Unit (RCU). The RCU will transmit the ADC samples from the readout buffer to ALICE data acquisition system.

Note that the light yield of $PbWO_4$ and the electronic noise level of the APD and CSP will be reduced a factor ~ 3 at a temperature of -25^oC as compared to those at in room temperatures. As a consequence PHOS crystals, APDs and CSPs are operated at the temperature of -25^oC with a fluctuation of 0.1^oC. It is achieved by a PHOS cooling system based on a liquid coolant Hydrofluoroether. The detector readout and trigger detectors are kept at a temperature of 15^oC. In addition, to keep the system stabilized at low humidity, nitrogen is fluxed through PHOS enclosure interior.

2.3.3 Intrinsic performance

The intrinsic performance of PHOS will be described in three parts: energy resolution, position resolution and time-of-flight resolution.

Energy resolution

The energy resolution for electromagnetic calorimeters can in general be parametrized as[89, 92]

$$\frac{\sigma_E}{E} = \sqrt{(\frac{a}{E})^2 + (\frac{b}{\sqrt{E}})^2 + c^2} \tag{2.1}$$

, where the energy E is in GeV, a represents the noise, b represents the stochastic term, and c represents the constant term. The stochastic term b takes into account the fluctuations in the electromagnetic shower and variations due to photoelectrons statistics, which includes, in particular, the light yield contribution and the APD excess noise factor. The term a includes contributions from preamplifier noise,

digitalization noise, and, in principle, pile-up noise, the latter being negligible in our tests. The constant term takes into account shower leakage at the back end of the crystals, inter-calibration errors, non-uniformity in the light collection and geometrical effects. In the ALICE Technical Proposal[97] and the PHOS Technical Design Report[89], these parameters are required to be less than 0.03, 0.03 and 0.01, respectively.

In Figure 2.14, the mean value and the energy resolution for sixteen 3×3 subset detectors is shown as a function of beam energy measured in the 2002 an 2003 beam tests. The dashed curve represents a fit to data by the Equation 2.1 with parameters $a = 0.013 \pm 0.0007$GeV, $b = 0.0358 \pm 0.002$ and $c = 0.0112 \pm 0.003$. Also shown in the figure is the PHOS requirement. The data indicate that the PHOS requirements are fulfilled with respect to the energy resolution.

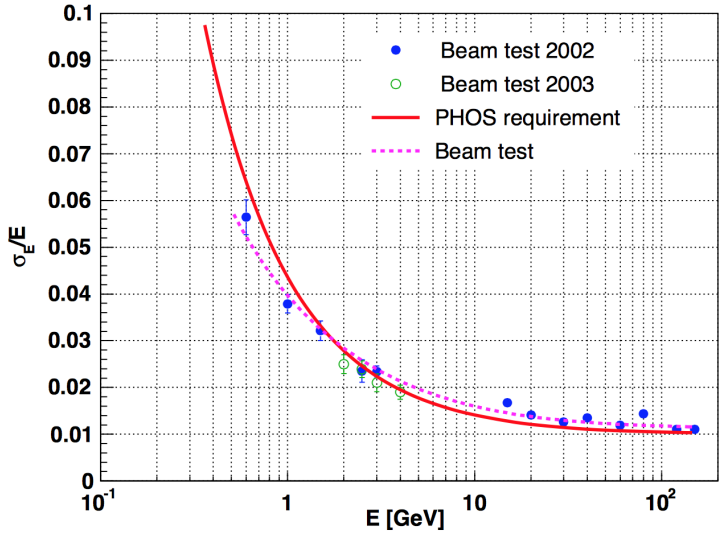

FIGURE 2.14: The measured mean value of the energy resolution for sixteen 3×3 subset detectors as a function of electron beam energy in the 2002 and 2003 beam tests. The dashed line is a fit to the data with Equation 2.1. The solid curve shows the PHOS requirement.

Position resolution

The position resolution of PHOS can be described by

$$\sigma_x = \sqrt{A^2 + \frac{B^2}{E}} \tag{2.2}$$

, where parameters A and B vary with the incident angle. 0^o, 3^o, 6^o, 9^o and random possible angles were simulated to measure the position resolution, Figure 2.15 shows the results.

Time-of-flight resolution

The measurement of the time-of-flight is needed to discriminate photons and $n\bar{n}$

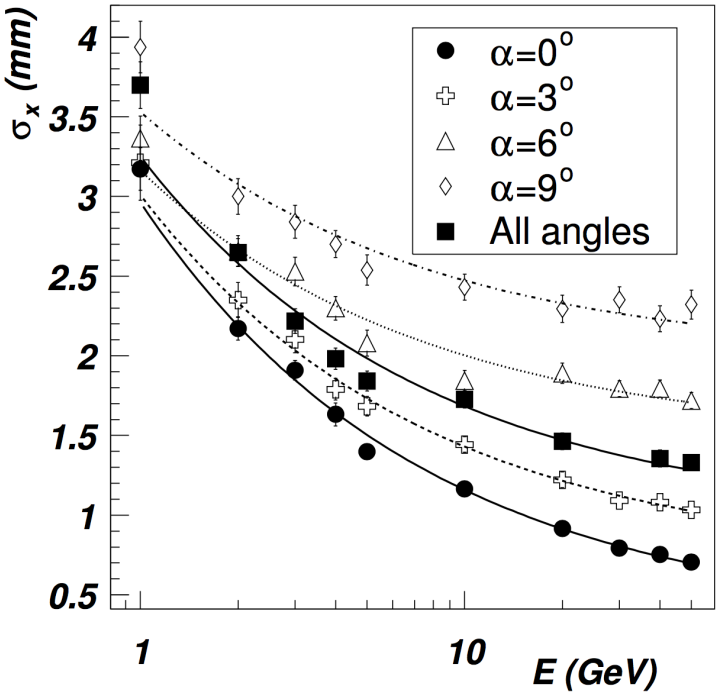

FIGURE 2.15: The position resolution versus the photon energy for the incidence angles on a PHOS module α=0°, 3°, 6° and 9° and the average for all possible incidences in the the ALICE layout.

annihilation because of their similar shower shapes, a resolution of 2 *ns* at 2 GeV is required.

The time-of-flight resolution is limited downwards by the intrinsic time-of-flight resolution of 500 *ps* of the $PbWO_4$ crystal. Other factors that influences the time-of-flight resolution is the charge collection time of the CSP, the electronic noise and the time constant of the shaping circuit. It can be shown that the time-of-flight resolution is inversely proportional to the energy and proportional to the square root of the time constant of the shaper

Chapter 3

Neutral Pion Analysis

This chapter is dedicated to the neutral pion analysis in p–Pb collisions at $\sqrt{s_{\mathrm{NN}}} = 7$ TeV. The analysis fundamentals part includes clusterization and neutral pion extraction. Then we will go through all the procedures of raw yield determination. Finally the invariant yield of π^0 is extracted by Monte Calo analysis.

3.1 Analysis fundamentals

This analysis aims to measure the π^0 invariant cross-section as a function of transverse momentum (p_{T}). The general strategy is to look in the channel $\pi^0 \to \gamma\gamma$ by measuring the two decay photons in the PHOS. This branching ratio accounts for approximately $98.823 \pm 0.034\%$ of all π^0 decays. The π^0 mass is 134.977 ± 0.001 MeV/c^2 and it's lifetime (τ) is $(8.52 \pm 0.18) \times 10^{-17}$ seconds, corresponding to $c\tau = 25.5$ nm. Therefore, effectively, every π^0 decays immediately after it's created. In contrast, the $\pi^{\pm}$ has a mass of 139.57 MeV/c^2 and a mean lifetime of ~ 260 μs leading to a $c\tau$ of ~ 7.8 m.

The mass and transverse momentum of the π^0 candidates are calculated as

$$m_{\pi^0} = \sqrt{2E_{\gamma_1}E_{\gamma_2}(1-\cos\theta)} \tag{3.1}$$

$$p_{T,\pi^0} = |\vec{p}_{T,\gamma_1} + \vec{p}_{T,\gamma_2}| \tag{3.2}$$

, where θ is the opening angle between the two photons.

It is vital to be able to spatially resolve each of the individual photons. If θ is too small then it's possible that the energy depositions in the calorimeter will overlap causing the photons to appear "merged." In such a case, the diphotons appear as a single high(er)

energy photon and the π^0 is lost. For a more detailed discussion of merging, see the descriptions of the clusterizer in Section 3.1.1.

Since there is no inherent way to determine whether cluster i and cluster j are from the same parent π^0 and should thus be paired together, the strategy is to combine *all* combinations of pairs of clusters and then statistically subtract the consequent background. By the mathematical fitting or using the mixing event technique (which construct the uncorrelated photon pairs from adjacent buffer events with the similar features), it allows us to subtract the background as well as to estimate the systematic uncertainty by comparing different extraction methods. For a more detailed discussion of background subtraction, see in Section **??**.

3.1.1 Clusterization

A cluster, resulted in when a crystal is fired by an incidental particle, is composed by a group of adjacent cells with an energy deposition above a threshold. Required by the PHOS physics motivation, the cluster reconstruction should fulfill:

1. Precise reconstruction of the incident particle position and energy deposit;
2. Separation of electromagnetic (γ and $e^{\pm}$) and hadronic showers;
3. Identification and unfolding two or more overlapping showers.

As follows, all of the techniques are discussed in details.

- **Cluster finding**

  Any cell with an energy larger than a minimal energy value E_1^{th} (the noise threshold) is considered as a seed of a new cluster. The cluster is formed when there are other cells around this one whose energy is greater than E_2^{th}. If one of the cells which belongs to the cluster has a energy much higher than all the other cells a value of E_3^{th}, the cell is tagged as a local maximum. The simulation study turns out that the procedure is poor sensitive to the adjustable parameters E_2^{th} and E_3^{th}. In principle, one incidence particle will generate one local maximum in the cluster, so that two or more local maximum mean there are superposition of multiple showers.

- **Cluster unfolding**

  The unfolding algorithm deals with the clusters containing multiple local maxima

with the most probability occurring in a high multiplicity environment. The basic idea is based on the knowledge of electromagnetic shower lateral distribution parameterized as

$$f(r,E) = e^{-r^4*(\frac{1}{2.32+0.26*r^4}+\frac{0.0316}{1+0.652*r^{2.95}})} \tag{3.3}$$

, where r is the distance from the cell center to the incident point, and E is the energy deposition in one cell relative to the total energy. Assume there are N local maxima from the cluster, the pulse height A_i^1 of the i^{th} cell is subdivided into A_i^1 , A_i^2 , ..., A_i^N following the formula:

$$A_i^k = A_i \times \frac{fr_{ik}, E_k}{\sum_{j=1}^{N} f(r_{ij}, E_j)} \tag{3.4}$$

More detailed on the cluster unfolding algorithms can be found in [89]. The procedure had been validated in simulation and real data. It demonstrates a good cluster unfolding capability to 25 GeV/c for PHOS.

- **Coordinates and energy reconstruction of an incident particle**

  The coordinates of the incident particle in the (x, z) plane are calculated using the center of gravity algorithm

$$\bar{s} = \sum_i s_i w_i / \sum_i w_i \tag{3.5}$$

  with a logarithmic weight

$$w_i = max[0, w_0 + log(e_i/E)] \tag{3.6}$$

  , where the parameter w_0 is empirically determined. Due to the effective depth of the shower which increases logarithmically with energy, the additional correction is taken into account by using the function:

$$\Delta_x(mm) = -[a \cdot ln(E(\text{GeV})) + \text{b}] \cdot \sin\alpha \tag{3.7}$$

  , where α is the angle between the normal to the detector and the incident particle. These parameters depend only on the radiation length of the detector material and are independent on the granularity. The cluster energy is the sum of energy of cells which belong to the cluster. For each pp collision, the primary vertex can be reconstructed by correlating hits in SPD. The resolution depends on the charged track multiplicity and is $0.1 \sim 0.3$ mm in the longitudinal and $0.2 \sim 0.5$ mm in the transverse direction. Knowing the cluster position, energy and direction from collision vertex, the particle four-momentum is reconstructed.

- **Shower shape**

  The shower shape analysis is an effective method to discriminate photons from the other charged hadrons. There are four main shower shape parameters: dispersion, two main axes and the sphericity as explained below.

  Shower dispersion

  The dispersion reflects the difference of the shower radial energy profile. It is calculated as:

$$D_s^2 = \frac{\sum_i w_i s_i^2}{\sum_i w_i} - (\frac{\sum_i w_i s_i}{\sum_i w_i})^2 \tag{3.8}$$

  , where s stands for the cell (x, z) coordinate, the w_i uses the same parameters as in Equation 3.5. Then the final dispersion of the cluster is $D = \sqrt{D_x^2 + D_z^2}$.

  Two main axes and sphericity of the shower

  On the surface of PHOS the two main axes (λ_0, λ_1) are calculated by constructing a 2×2 sphericity tensor and solving its eigenvalues:

$$S_{xx} = \sum_i E_i x_i^2 \tag{3.9}$$

$$S_{xz} = S_{zx} = \sum_i E_i x_i z_i \tag{3.10}$$

$$S_{zz} = \sum_i E_i z_i^2 \tag{3.11}$$

  , where x_i, z_i are the coordinates of cell i^{th} of the cluster, major axis λ_0 and minor axis λ_1 are shown in Figure 3.1. Then the cluster sphericity is defined as:

$$S = \frac{|\lambda_0 - \lambda_1|}{\lambda_0 + \lambda_1} \tag{3.12}$$

3.1.2 Neutral pion extraction

- **Mathematical fitting**

  A direct way to extract the signal π^0 from the real events consists in using mathematical fit. However, the method is only valid under two prerequisites: a) the signal to background ratio (S/B) or the significance $(S/\sqrt{S+B})$ stays at an acceptable level; b) the shape of the background has been well understood.

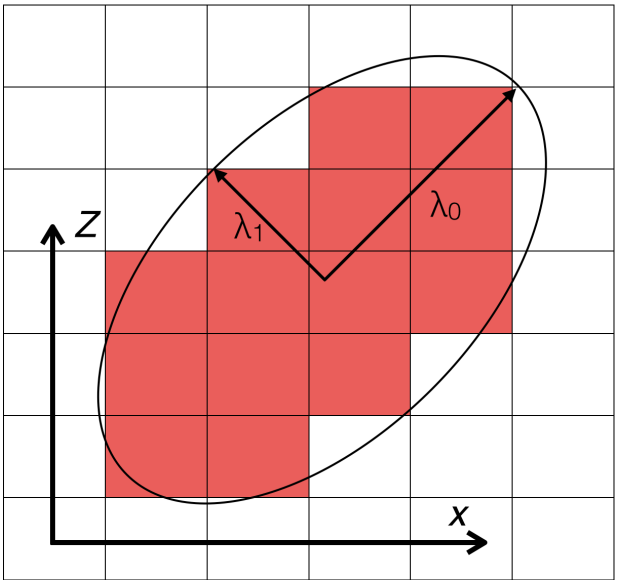

FIGURE 3.1: Ellipse cluster shower on the surface of the PHOS modules

As show in Figure 3.2, the π^0 peak position and its combinatorial background can be fitted by a Gaussian plus a polynomial function

$$f(m) = A \cdot e^{\frac{-(m-\bar{m})^2}{2\sigma}} + a_0 + a_1 m + a_2 m^2 + \dots \tag{3.13}$$

, where the Gaussian function describes the signal, while the polynomial function describes the background. The number of π^0 is counted by the integration of the Gaussian fitting function as:

$$N = \frac{A \cdot \sigma \cdot \sqrt{2\pi}}{\Delta m} \tag{3.14}$$

and the error is calculated by propagating the errors from the above formula:

$$N_{error} = N \cdot \sqrt{(\frac{eA}{A}^2) + (\frac{e\sigma}{\sigma})^2} \tag{3.15}$$

, where eA and $e\sigma$ denote the fit uncertainties of A and σ separately. An additional Crystal Ball parameterization includes a Gaussian core portion and a power-law tail below a certain threshold as:

$$f(x) = N \begin{cases} exp(-\frac{(x-\bar{x})^2}{2\sigma^2}) & \text{if } \frac{x-\bar{x}}{\sigma} > -\alpha \\ A(B - \frac{x-\bar{x}}{\sigma})^{-n} & \text{if } \frac{x-\bar{x}}{\sigma} \leq -\alpha \end{cases} \tag{3.16}$$

, where $A = (\frac{n}{|\alpha|}(^n \cdot exp(-\frac{\alpha^2}{2})$ and $B = \frac{n}{|\alpha|} - |\alpha|$. With this fitting function plus a polynomial function, the distribution can be fitted quite well. It offers us a crosscheck to other methods.

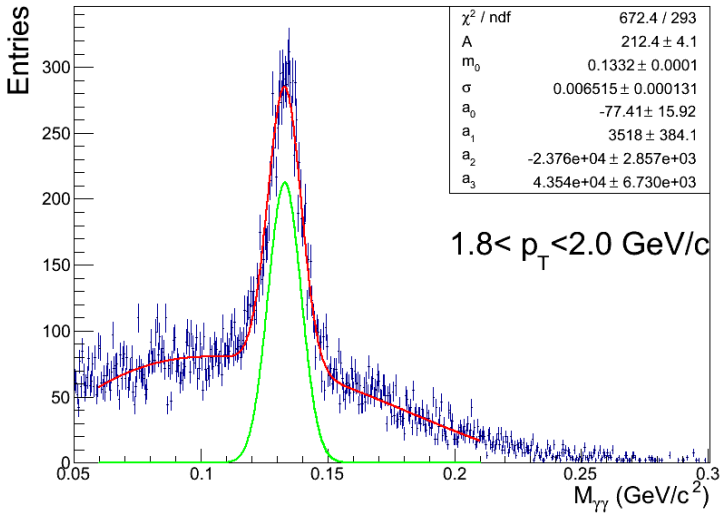

FIGURE 3.2: Signal extraction for 2γ real distribution by using Gaussian + second order polynomial as fitting function

- **Event mixing technique**

  Another way to subtract the background is by using of mixing event procedure. This becomes crucial in heavy-ion collisions due to the smaller signal-to-background ratio. The general procedure is shown in Figure 3.3 and described as below:

  - Real events: Loop the photon pairs in one event to get the signal+background $f_{real}(p_{\mathrm{T}}, m_{2\gamma})$.
  - Mixing events: Select events with similar properties (centrality, vertex etc.). Then pick up a photon from the current event and a photon from the other events to construct the uncorrelated photon pairs $f_{mix}(p_{\mathrm{T}}, m_{2\gamma})$. Usually the size of event buffer is about $10 \sim 100$ and $5 \sim 10$ in pp & p–Pb and AA collisions separately depending on the computing resource.
  - Normalization of the mixed background. Because of the two multiple photon pair combinations, it is necessary to normalize the mixed background properly to be subtract from the real events. Based on the fact that the background outside of the π^0 nominal mass should have a similar shape. In each p_{T} bin, we first fit the ratio of the two invariant mass distributions

    $$f_{ratio}(m_{2\gamma}) = \frac{f_{real}(m_{2\gamma})}{f_{mix}(m_{2\gamma})} \tag{3.17}$$

    by a first/second order polynomial function in a range which should be outside of the π^0 nominal mass. Then we use this function to normalize the mixed background.

- Counting the numbers: The background is subtracted as

$$f_{sig}(m_{2\gamma}) = f_{real}(m_{2\gamma}) - f_{ratio}(m_{2\gamma}) * f_{mix}(m_{2\gamma}) \tag{3.18}$$

The number of π^0 is calculated by the integration of $f_{sig}(m_{2\gamma})$ in their nominal mass window ($\bar{m} \pm 3\sigma$):

$$N = \int_{m_0-3\sigma}^{m_0+3\sigma} f_{sig}(m_{2\gamma}) dm_{2\gamma} \tag{3.19}$$

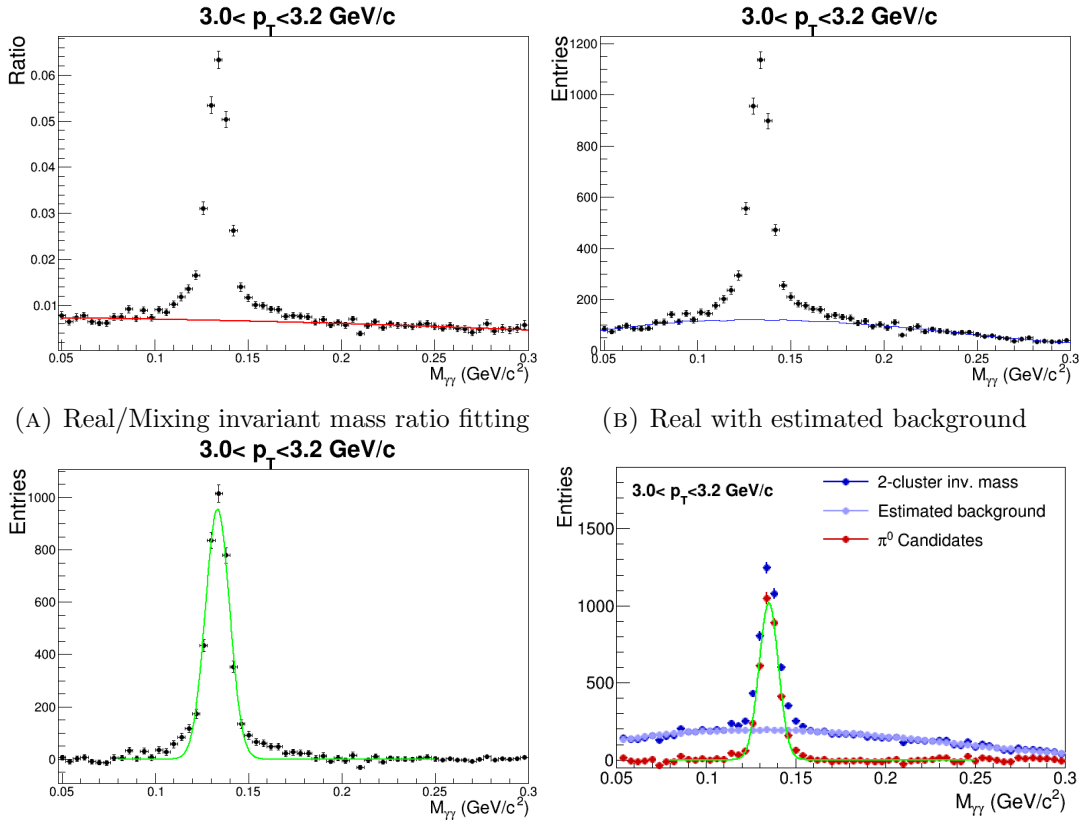

(A) Real/Mixing invariant mass ratio fitting

(B) Real with estimated background

(C) π^0 candidates fitting

(D) Neutral pion extraction

FIGURE 3.3: The procedure of the signal extraction at 3.0 GeV/c $< p_T <$ 3.5 GeV/c by event mixing technique.

3.2 Raw yield determination

This section presents the analysis of p–Pb collisions data at 5.02 TeV. About 90 million min-bias events are selected via the standard physics selection and data quality assurance. Then we follow the cluster and cluster-pair selection used in pp analysis. The raw yield of neutral pions are extracted by using invariant mass analysis.

3.2.1 Data sample, event selection and QA

The p–Pb data at $\sqrt{s_{\rm NN}} = 5.02$ TeV has been collected during the LHC13b and LHC13c run periods for min-bias events. And this analysis is done with the third reconstruction pass (pass3) with 27 runs in AOD. There are 4 bad runs for PHOS which will be excluded by following QA analysis.

The trigger detector V0 is used to select the min-bias events. It accepts events which have at one hit in each V0 beam counters(V0A & V0C). To subtract the min-bias events background, such as from beam-gas or pileup events, the offline analysis follows the official physics selection (AliPhysicsSelection [98] in AliRoot) by ALICE analyzers. Besides, for p-Pb analysis, number of tracks participating to vertex, vertex z coordinate and SPD and TPC vertex deviation are used to select events with proper vertex. Pile-up events with multiple vertexes are rejected.

After event selection strategy, the data quality assurance (QA) should be studied to choose the appropriate data sample for PHOS. The cluster with a energy > 300 MeV/c and digit multiplicity > 2 is selected as a photon candidate for π^0 reconstruction. In addition, a group of criteria based on the average characterization in a event is defined for the QA analysis:

- Average value of cluster energy;
- Average value of the number of cells per reconstructed cluster;
- Average value of the number of reconstructed clusters per event.

Figure 3.4 shows most of runs are stable in each module but some runs have abnormal behavior. Run 195596 is empty because this run does not include PHOS. We can notice that run number 195346, 195532 and 195675 are abnormally compared to other runs. These runs will cause a negative effect for results. Then these 4 runs will be excluded in this analysis.

3.2.2 Cluster selection

When PHOS is well studied in pp collisions, we follow the pp analysis cluster selection cuts for the p–Pb physics analysis as following:

- **Energy of cluster** $E_{cluster} > 0.3$ GeV/c**.** The hadron deposits its energy through the ionization loss process corresponding to a minimal energy 230 MeV in calorimeters. Also there are fractional cluster energies from electronic noise. Here we set

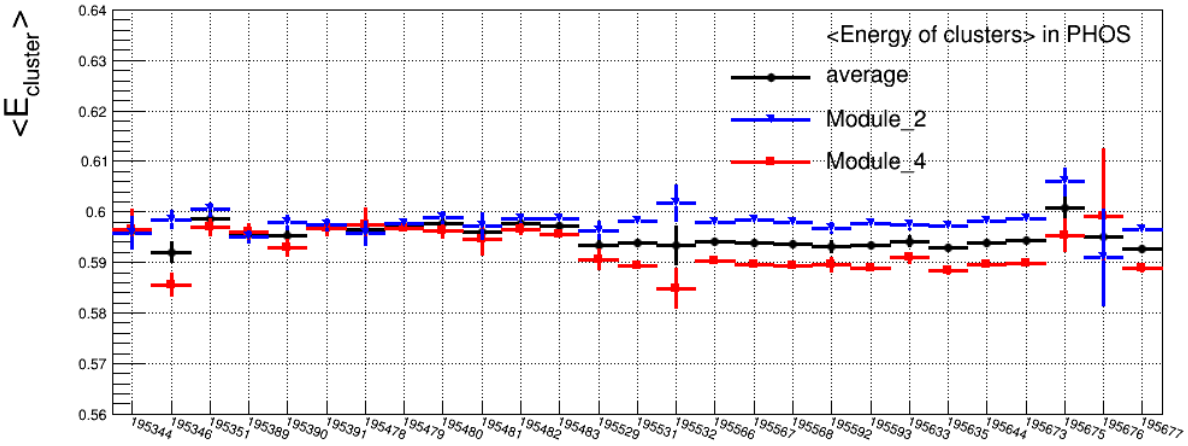

(A) Average value of cluster energy

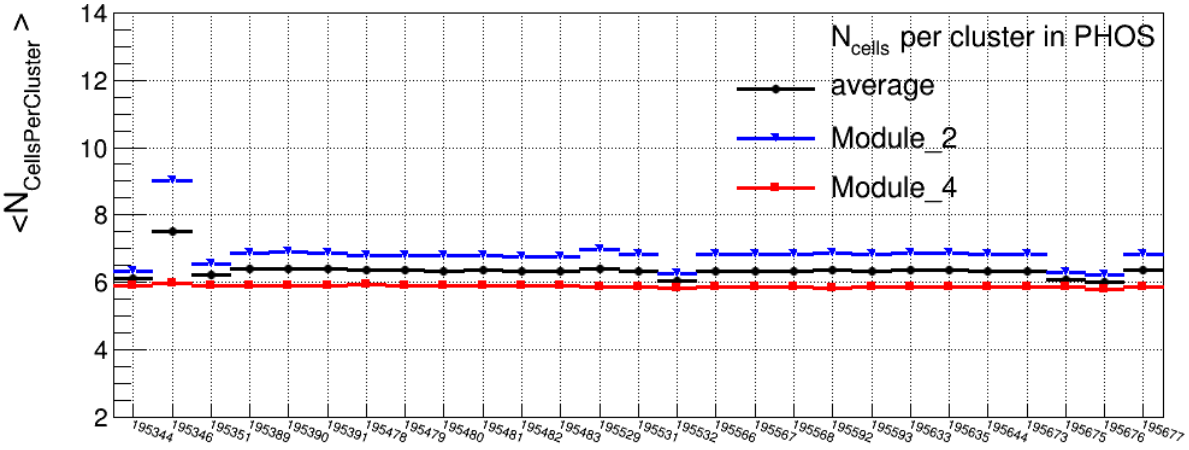

(B) Average value of the number of cells per reconstructed cluster

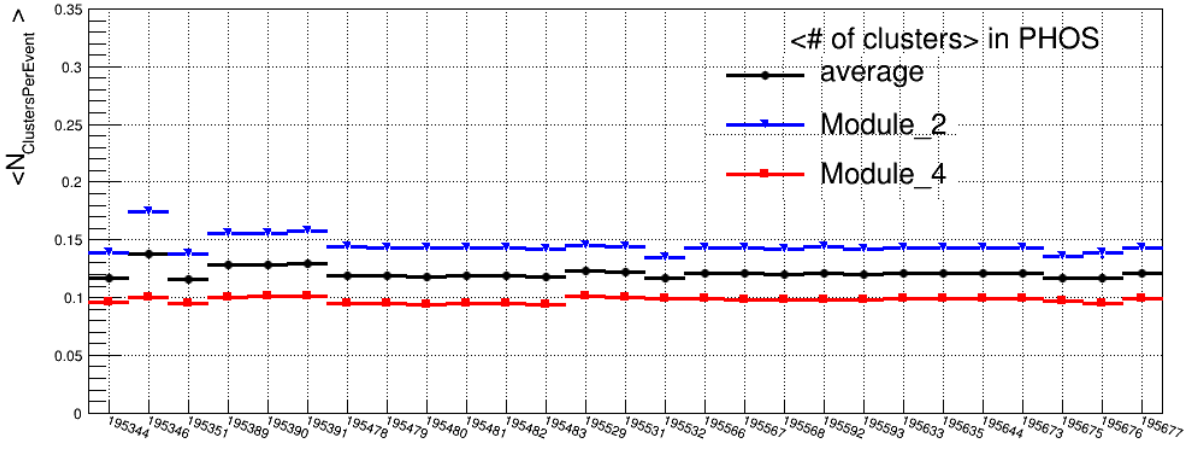

(C) Average value of the number of reconstructed clusters per event

FIGURE 3.4: Run QA of PHOS in p–Pb collisions at $\sqrt{s_{\mathrm{NN}}} = 5.02$ TeV

the cuts $> 0.1, 0.3, 0.5, 0.7$ and 1 GeV/c to estimate the influence on π^0 spectra. In the final analysis, the energy of cluster which is larger than 300 MeV/c are selected to suppress the hadronic background.

- **Cell multiplicity of the cluster** $N_{cells} > 2$**.** It is firstly used to suppress the background by minimum ionizing particles and hadron. In addition, the high energy charged hadrons deposit small part of their energy in calorimeters but with a larger spread. Finally, there are occasional clusters with a small number of cell multiplicity but with a large energy, which may be caused by the punch-through effect or non-physics source.

- **Distance to bad channels > 2.5 crystals.** The energy of incident particle (γ) will be partly lost or changed in case there are some bad channels among the fired channels. By using the distance to bad channel cut will remove this contribution to keep the integral information of the photon cluster. Figure 3.5 show the cluster distribution in the detector transverse.

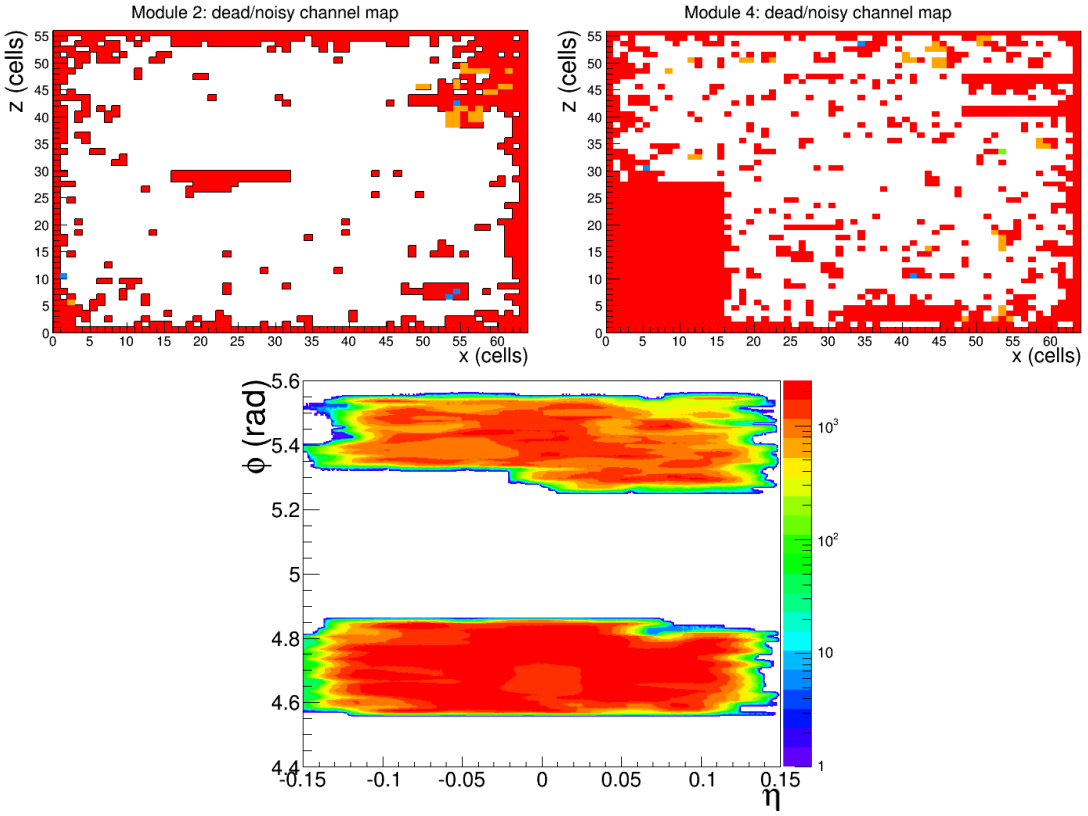

FIGURE 3.5: Upper: PHOS bad channel maps; Lower: PHOS cluster distribution with distance to bad channels cut in $\eta - \phi$ axes

- **Major axis of the cluster shower ellipse** $\lambda_0 > 0.2$ is to remove the exotic clusters.

- **PHOS cluster timing** $|TOF| < 100\ ns$ is to remove the pile-up events from next bunch crossing. For the p–Pb collisions, time window between two bunches was alternated at 200, 225 ns. In the Figure 3.6, there are double peaks at 200 ns and 225 ns, and peak at 424 ns. And PHOS cluster timing cut will remove all the other bunch crossing and have good statistics for analysis.

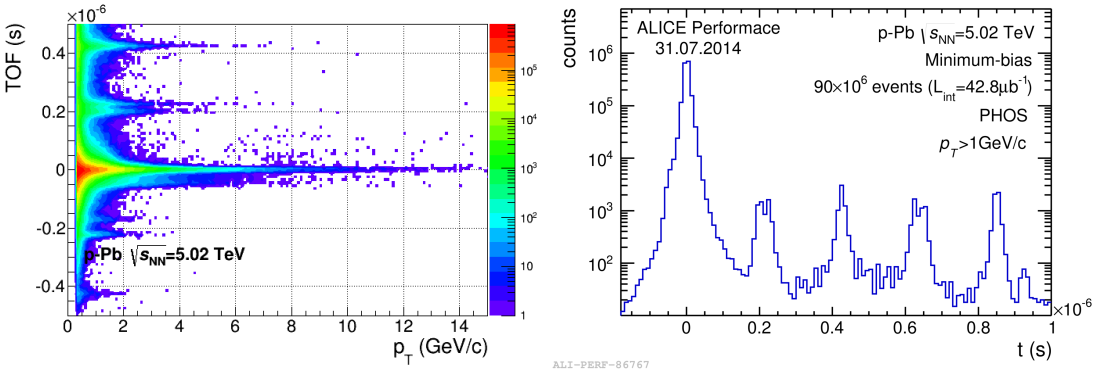

FIGURE 3.6: Left: PHOS cluster TOF distribution as a function of p_{T}; Right: PHOS cluster TOF distribution with transverse momentum $p_{\mathrm{T}} > 1$ GeV/c

- **Particle identification** is critical for the photon selection and the photon physics analysis where we should unambiguously know the particle ID. However, for the neutral pion measurements, there is no effect on the extraction of the resonance peak, and thus we will not use it here.

3.2.3 π^0 raw yield extraction

We first construct the 2 dimensional histogram ($m_{2\gamma}$, p_{T}), and then extract the number of π^0 in each p_{T} bin. Due to some correlated background originating from the photon conversion, or some other physics processes such as the jet fragmentation, flow effect and HBT correlations, there are some combinatorial background around the π^0 peak at low p_{T}.

The procedure by using the mixing event technique to subtract the background has been introduced in the Section 3.1.2. In p–Pb collisions, there is no strong combinatorial background at high p_{T}(¿6 GeV/c) in real events and what we are concerned with is the lower p_{T} contribution to the π^0 peak. In this analysis, the buffer size of mixed events is set to 100, which is larger than in PbPb collisions, in order to construct enough statistics at larger p_{T} to fulfill the analysis requirement. Ratio real/mix measured in p–Pb collisions at $\sqrt{s_{\mathrm{NN}}} = 5.02$ TeV are fitted with a Gaussian with a second order polynomial function. The ratio is not constant outside the nominal π^0 mass window because of the presence of the uncorrelated background. The real distributions and normalized backgrounds are shown in Figure 3.7, Figure 3.8 and Figure 3.9.

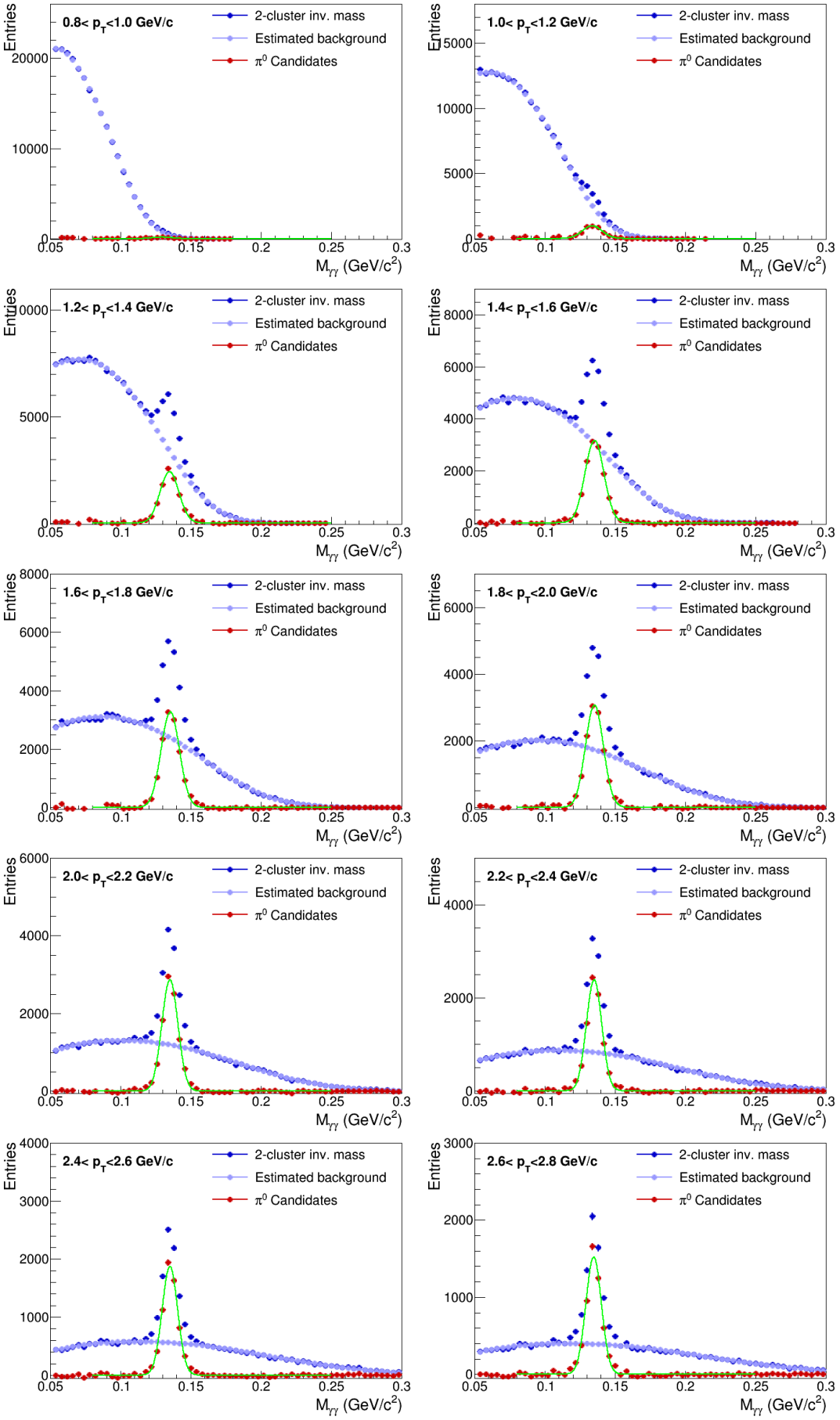

FIGURE 3.7: PHOS in p–Pb collisions at $\sqrt{s_{\mathrm{NN}}} = 5.02$ TeV: Background subtraction process of π^0 data analysis at $0.8 < p_{\mathrm{T}} < 2.8$ GeV/c

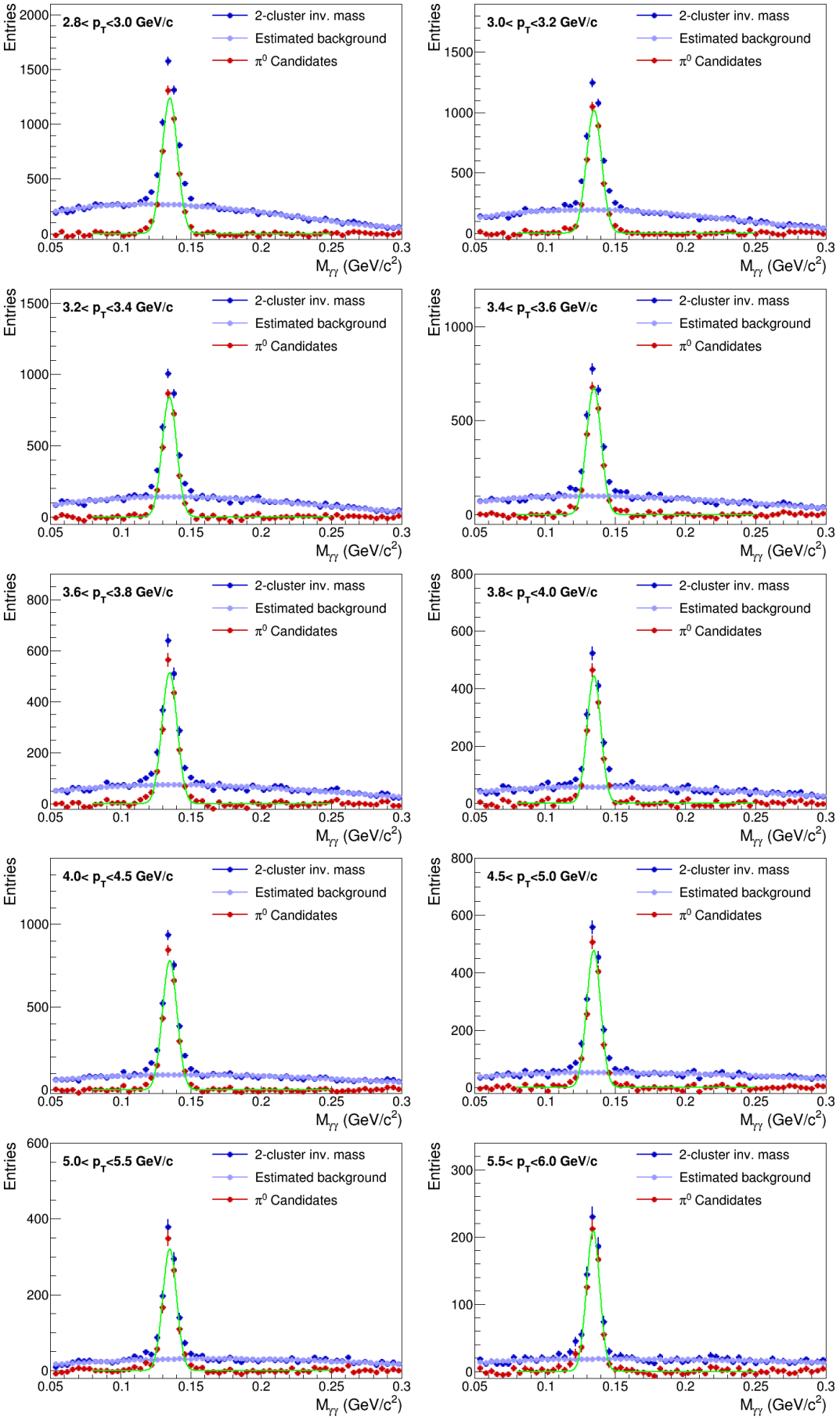

FIGURE 3.8: PHOS in p–Pb collisions at $\sqrt{s_{\mathrm{NN}}} = 5.02$ TeV: Background subtraction process of π^0 data analysis at $2.8 < p_{\mathrm{T}} < 6.0$ GeV/c

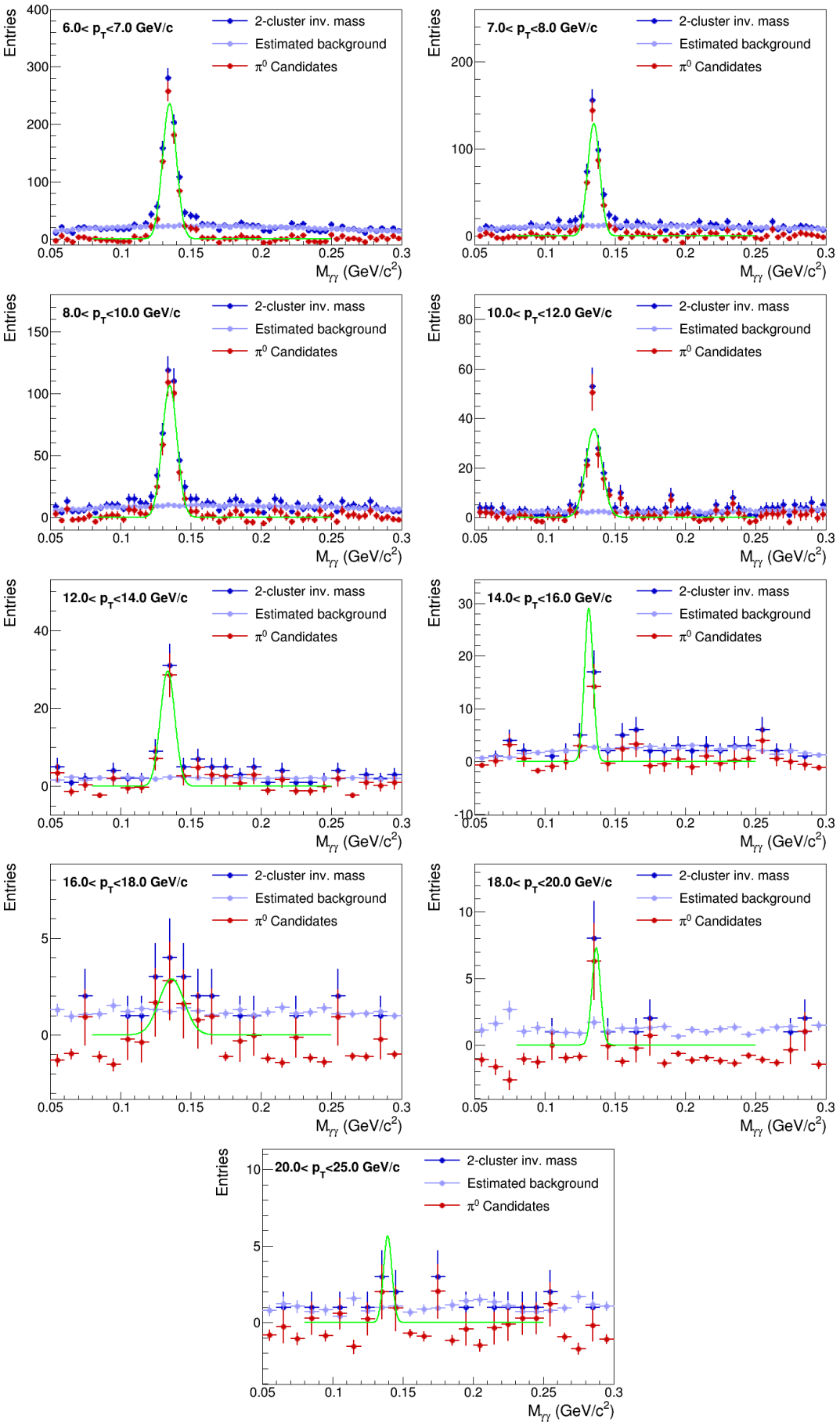

FIGURE 3.9: PHOS in p–Pb collisions at $\sqrt{s_{\mathrm{NN}}} = 5.02$ TeV: Background subtraction process of π^0 data analysis at $6.0 < p_{\mathrm{T}} < 25.0$ GeV/c

3.2.4 Summary

This chapter has been presenting the analysis of p–Pb collisions at 5.02 T eV with PHOS detector. 23 runs with 90 million events have analyzed. The raw spectra are shown in Figure 3.10 for π^0 by using the cuts:

a) $E_{Cluster} > 0.3$ GeV/c;

b) $N_{Cells} > 2$;

c) Distance to bad channel cut is larger than 2.5 crystals size;

d) Major axis of cluster shower ellipse $\lambda_0 > 0.2$;

e) PHOS cluster timing $|TOF| < 100$ ns;

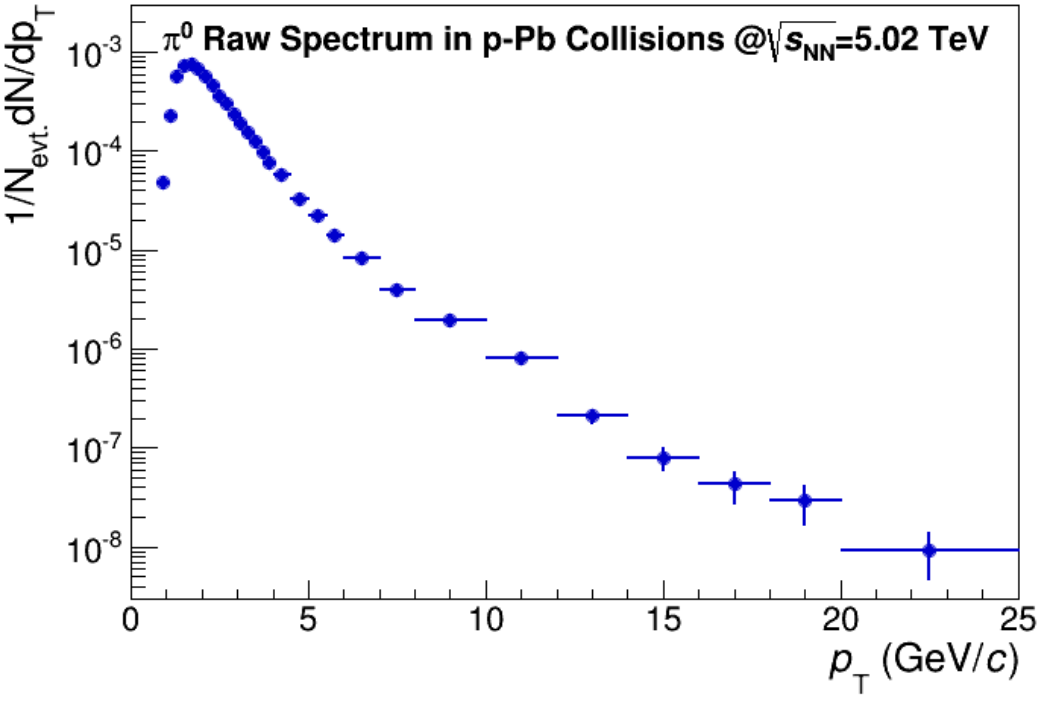

FIGURE 3.10: π^0 raw yield by the invariant mass of 2γ in PHOS with p–Pb collisions at $\sqrt{s_{\rm NN}} = 5.02$ TeV. The spectrum is normalized to the total number of events.

3.3 Monte Carlo analysis

3.3.1 MC fundamentals

In principle, the GEANT simulation should describe the detector response in totality. However, this premise must not be taken for granted. The calibration between data and

MC must be properly accounted for in order to trust that the MC is accurately describing the PHOS. One way to test MC is making comparison of π^0 peak width and position between data and MC simulations. Figure 3.11 shows reconstructed π^0 peak width and position are well matched from 2 GeV/c to 16 GeV/c. In this section, all of the analysis are based on all available Monte Carlo data sample (periods: LHC13b2_efix_p[1 – 4]) for p–Pb collisions at $\sqrt{s_{\rm NN}}$ = 5.02 TeV with 77M min-bias events.

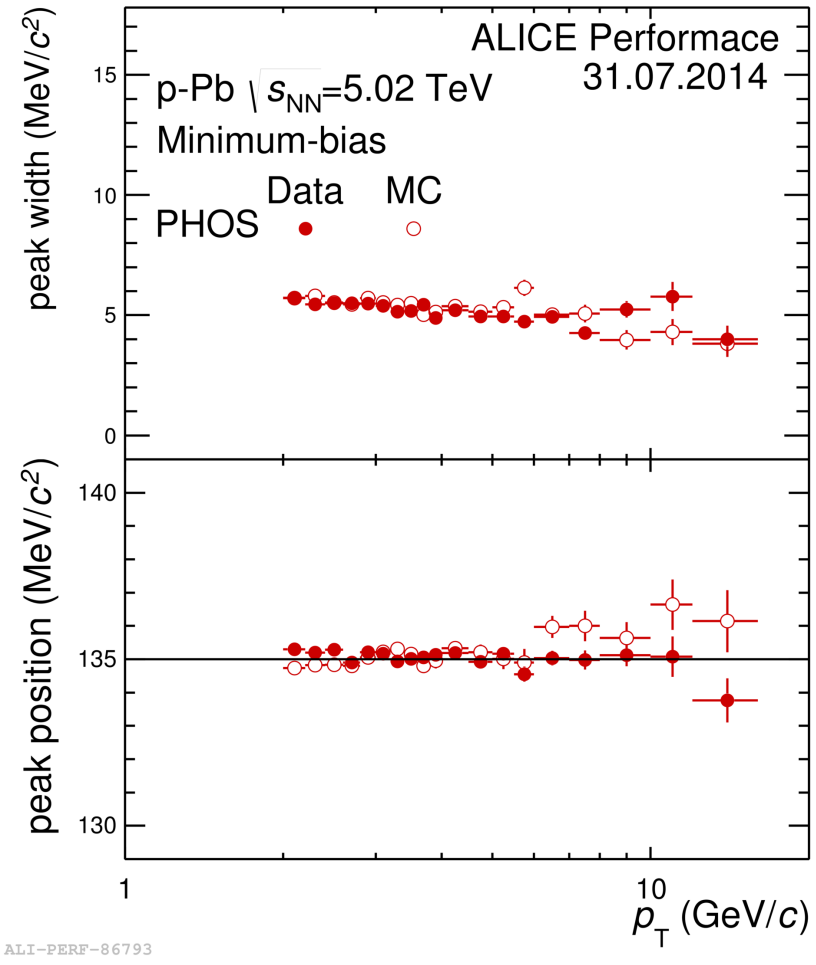

FIGURE 3.11: Position (lower) and width (upper) of the π^0 peak on invariant mass spectrum in data and MC.

In order to estimate the correction factors(in Section 3.3.2) the same analysis as in real data has been performed on simulated data. However, each cluster is verified using the MC information and it has been checked that they originate from the same particle π^0. In the Figure 3.12, the reconstructed π^0 (gray dots) is reconstructed by using two clusters to build invariant mass and removing combinatorial background via mixed events(the same way as real data); the inclusive π^0 (black dots) is reconstructed via invariant mass coming from the two clusters traced back to the same π^0; the pure π^0 (red dots) is inclusive π^0 which traces back via photonic clusters($\pi^0 \rightarrow \gamma\gamma$); the converted π^0 (blue dots) is inclusive π^0 which traces back via $\pi^0 \rightarrow \gamma\gamma$(at least one photon converting into

e^+e^- in the materials). Figure 3.12 shows the MC simulation is self-consistent and all of the correction factors are appropriate for the raw yield in real data.

3.3.2 π^0 spectra corrections

After having obtained the raw yield of the mesons several corrections need to be applied. At first the contribution from secondary π^0 from weak decay or hadronic interactions in the detector material need to be removed from the reconstructed raw neutral pions yield. Afterwards, corrections for the geometrical acceptance and reconstruction efficiency are applied.

The first physics goal with PHOS aim at measuring the invariant cross section of light neutral mesons in p–Pb collisions as an intermediate step between Pb–Pb and benchmark pp collisions to disentangle hot and cold nuclear matter, expressed by the formula quoted below:

$$E\frac{d^3\sigma}{dp^3} = \frac{1}{2\pi}\frac{1}{p_{\mathrm{T}}}\frac{\sigma_{MB}}{N_{evt.}}\frac{1}{BR}\frac{1}{A_{\pi^0}\times\epsilon_{reco.}}\frac{\Delta N_{\pi^0}}{\Delta p_{\mathrm{T}}\Delta y} \tag{3.20}$$

, where $N_{evt.}$ is the number of events for normalization, σ_{MB} is the cross section for the MB_{OR} trigger, the $A_{\pi^0}\times\epsilon_{reco.}$ is the correction factor from geometrical acceptance and reconstruction efficiency, the BR is the branching ratio of the decay $\pi^0\to\gamma\gamma$, and N_{π^0} is the reconstructed raw yield for π^0 within the pseudorapidity range [-0.5, 0.5] and the transverse momentum bin Δp_{T} without secondary π^0 contamination.

- **Feed-down correction**

  In order to extract exclusively the primary neutral pions the contributions from secondary π^0 from weak decays or hadronic interactions need to be removed from the π^0 raw yield. This correction has been evaluated using the same MC simulations, which have been used for efficiency and acceptance calculations. The decay $K^0_s\to\pi^0\pi^0$ with a branching ratio of BR = 30.7% represents the largest source of the secondary neutral pions. Figure 3.13 shows the fraction of all secondary pions or secondary pions from K^0_s decays to the all reconstructed neutral pions in p–Pb collisions at $\sqrt{s_{\mathrm{NN}}}$ = 5.02 TeV. These distributions have been obtained using all MC simulations for p–Pb collisions at $\sqrt{s_{\mathrm{NN}}}$ = 5.02 TeV.

  However, there are less K^0_s in the official MC simulations than in the real data. Additional π^0 from K^0_s from data compared to MC are subtracted by scaling the fraction of π^0 from K^0_s in the MC by the factor between the K^0_s in data and MC

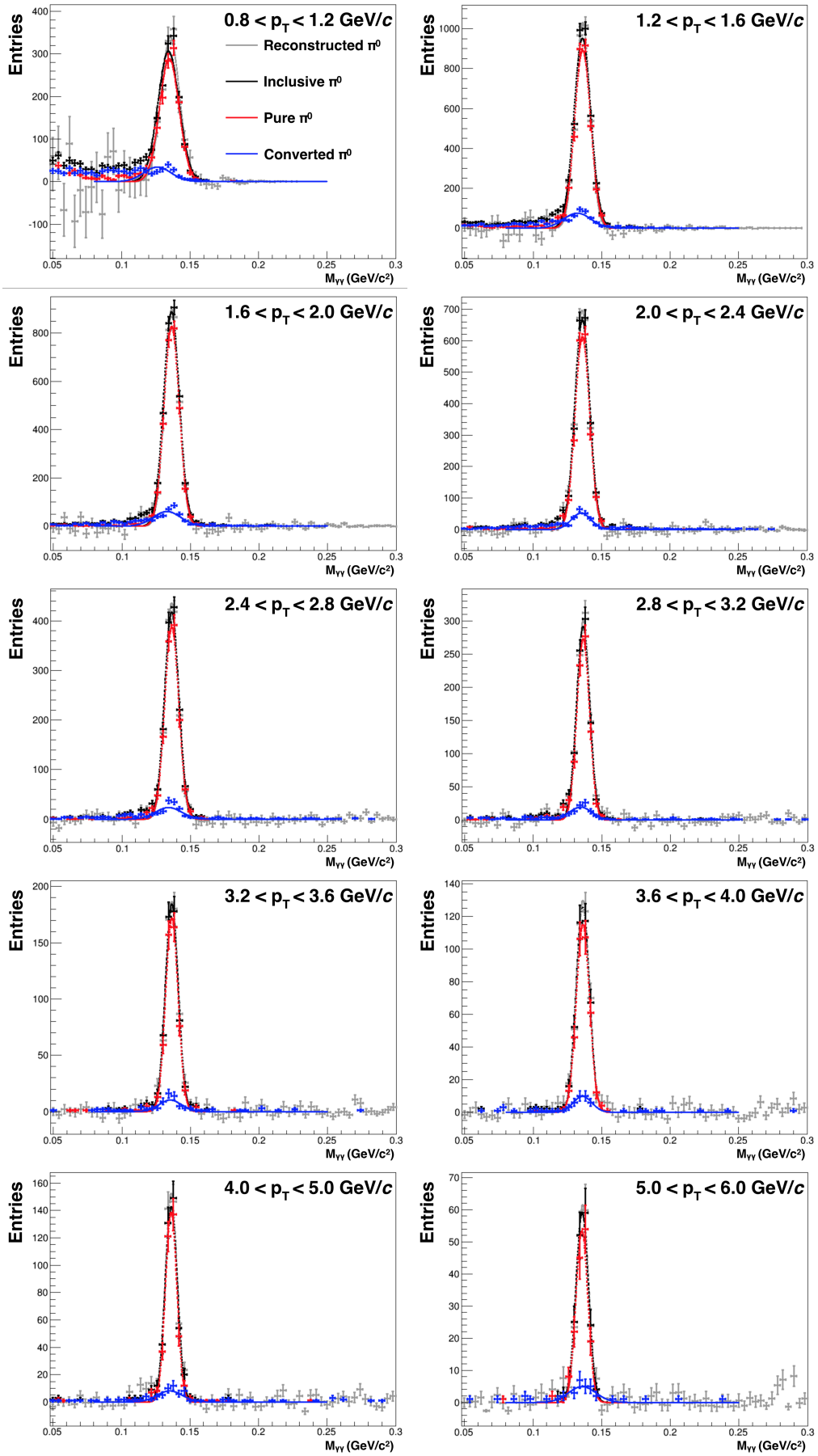

FIGURE 3.12: Self-consistent check for Monte Carlo simulations by using different π^0 reconstruction techniques

expressed by the formula quoted below:

$$invariant\ \pi^0\ yield = raw\ yield(1 - A - B)\frac{1}{A_{\pi^0} \times \epsilon_{reco.}} \tag{3.21}$$

, where

$$A = \frac{secondary\ \pi^0\ reconstructed\ in\ PHOS}{all\ \pi^0\ reconstructed\ in\ PHOS} \tag{3.22}$$

$$B = (\frac{1}{0.62} - 1) \cdot \frac{secondary\ \pi^0 \leftarrow K_s^0\ reconstructed\ in\ PHOS}{all\ \pi^0\ reconstructed\ in\ PHOS} \tag{3.23}$$

, and factor B is for the additional $\pi^0 \leftarrow K_s^0$ in data compared to MC.

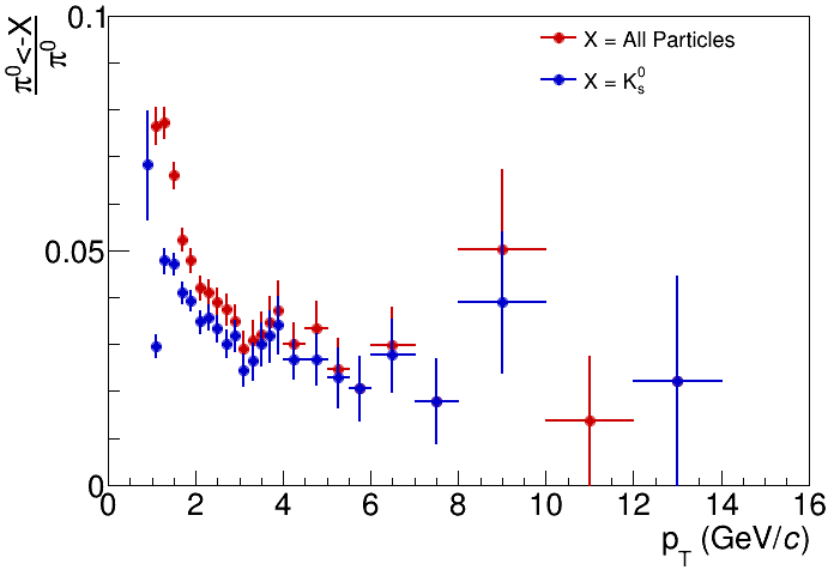

FIGURE 3.13: Ratio of reconstructed secondary π^0 from K_s^0 (blue dots) or all secondary π^0 (red dots) to reconstructed neutral pions.

- **Acceptance and reconstruction correction**

After the correction for secondary neutral pions the remaining primary raw yield of the π^0 meson needs to be corrected for detector acceptance and reconstruction efficiency. Both quantities are calculated using all available Monte Carlo simulations with generator DMPJET for the p–Pb collision systems at $\sqrt{s_{\rm NN}} = 5.02$ TeV.

The geometrical acceptance A_{π^0} (Equation 3.24) is defined as the ratio of primary π^0 within $|y| < 0.5$ and $0^{\rm o} < \varphi < 360^{\rm o}$, whose daughter particles are within the fiducial acceptance ($|\eta| < 0.135$ and $260^{\rm o} < \varphi < 320^{\rm o}$), over all π^0 generated in the same rapidity and φ window. The π^0 reconstruction efficiency $\epsilon_{\rm reco.}$ (Equation 3.25) is defined as the ratio of π^0 reconstructed within PHOS over π^0 within

$|y| < 0.5$ and $0^{o} < \varphi < 360^{o}$, whose daughter particles are within the fiducial acceptance ($|\eta| < 0.135$ and $260^{o} < \varphi < 320^{o}$).

$$A_{\pi^0} = \frac{N^{\text{prim.}}_{\pi^0} \text{ (its daughters within } |\eta| < 0.135 \text{ and } 260^{o} < \varphi < 320^{o})}{N^{\text{prim.}}_{\pi^0} \text{ within } |y_{\pi^0}| < 0.5 \text{ and } 0^{o} < \varphi_{\pi^0} < 360^{o}} \tag{3.24}$$

$$\epsilon_{\text{reco.}} = \frac{N^{\text{reco.}}_{\pi^0} \text{ within PHOS}}{N^{\text{prim.}}_{\pi^0} \text{ (its daughters within } |\eta| < 0.135 \text{ and } 260^{o} < \varphi < 320^{o})} \tag{3.25}$$

In Equation 3.20, $A_{\pi^0} \times \epsilon_{reco.}$ is the correction factor from geometrical acceptance and reconstruction efficiency expressed as following:

$$A_{\pi^0} \times \epsilon_{\text{reco.}} = \frac{N^{\text{reco.}}_{\pi^0} \text{ within PHOS}}{N^{\text{prim.}}_{\pi^0} \text{ within } |y_{\pi^0}| < 0.5 \text{ and } 0^{o} < \varphi_{\pi^0} < 360^{o}} \tag{3.26}$$

In the Figure 3.14, the min-bias event simulation limits $A_{\pi^0} \times \epsilon_{\text{reco.}}$ to reach high p_{T} due to the low statistics.

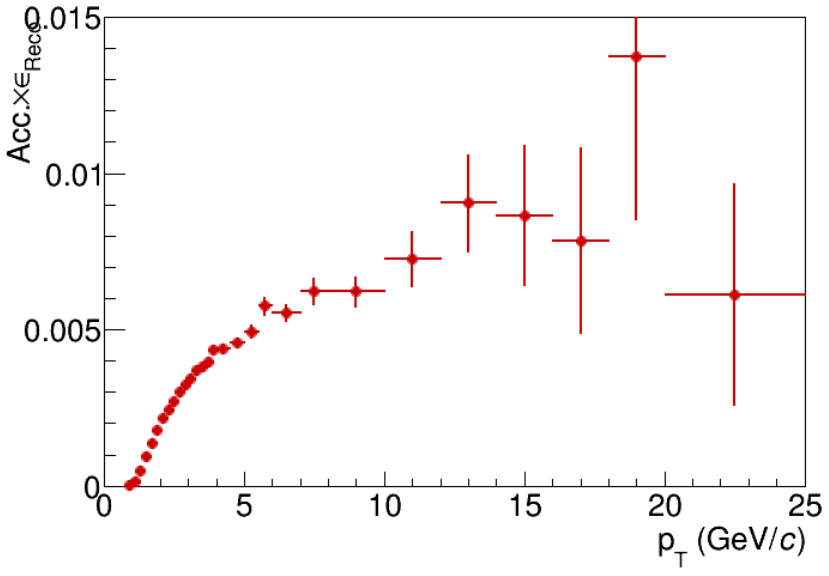

FIGURE 3.14: π^0 reconstruction efficiency and acceptance correction

Chapter 4

Results and Outlook

In this last chapter, the final physics results of π^0 production yield are presented. Comparing the invariant yield by others, we get the conclusions and outlook on the first measurement with ALICE PHOS.

4.1 Results

The raw spectrum of π^0 after the correction of the geometrical acceptance, reconstruction efficiency and the branching ratio is shown in Figure 4.1. There are four individual π^0 analysis at PHOS:

- Tsubasa's analysis correction part: LHC13b2_efix[1] for $p_{\mathrm{T}} < 7$ GeV/c and LHC13e7[2] with weight for $p_{\mathrm{T}} > 7$ GeV/c
- Boris's analysis correction part: LHC13b2_efix for $p_{\mathrm{T}} < 7$ GeV/c and single π^0 simulation for $p_{\mathrm{T}} > 7$ GeV/c
- Dmitri's analysis correction part: LHC13b2_efix for $p_{\mathrm{T}} < 7$ GeV/c and single π^0 simulation for $p_{\mathrm{T}} > 7$ GeV/c
- This analysis correction part: LHC13b2_efix for full p_{T} region

The invariant yield of π^0 in ALICE with p–Pb at $\sqrt{s_{\mathrm{NN}}} = 5.02$ TeV is well matched with others at $p_{\mathrm{T}} < 7$ GeV/c. Due to the limited statistics at $p_{\mathrm{T}} > 7$ GeV/c, the result fluctuates with p_{T}.

[1] LHC13b2_efix: min-bias simulation
[2] LHC13e7: added signal simulation

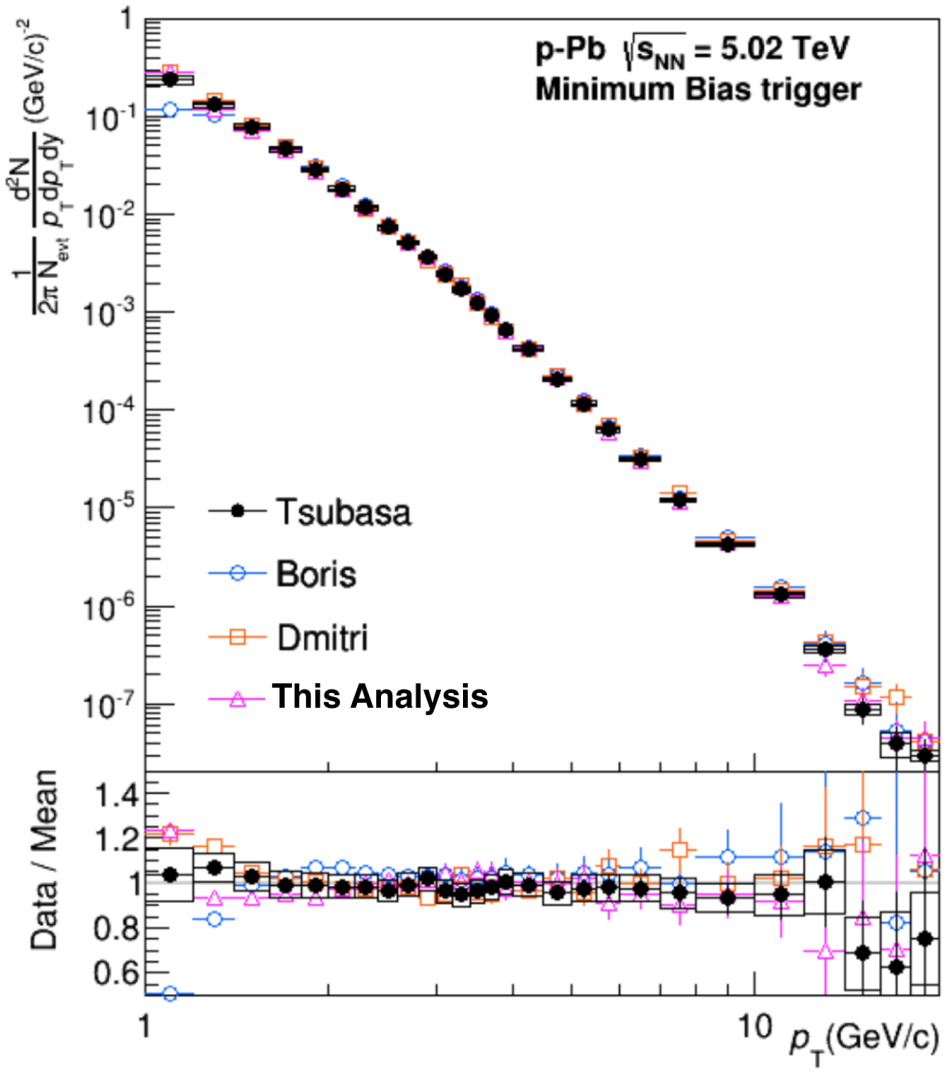

FIGURE 4.1: This analysis result: π^0 invariant yield measured in ALICE with p–Pb at $\sqrt{s_{\rm NN}} = 5.02$ TeV (triangle pink point), compared to the other three analysis.

4.2 Outlook

In this thesis, the strategy of the neutral pions measurement have been studied. Followed by the first p–Pb data-taking with ALICE at the LHC, we first understood our PHOS and made it work. Based on the statistics collected in p–Pb collisions at $\sqrt{s_{\rm NN}} = 5.02$ TeV , π^0 can be measured with a $p_{\rm T}$ range from 0.8 GeV/c to 25 GeV/c. The production yield is obtained for π^0 compared with three individual analysis. The result presents good matching at $p_{\rm T} < 7$ GeV/c. This measurement is an intermediate step for the pp and Pb–Pb analysis to disentangle the nuclear matter properties.

ALICE now has started the new production since June, 2015 and will continue the data-taking with pp and PbPb collisions till the end of 2015. More physics data will be collected under the designed luminosity. Then ALICE PHOS will take the chance to get

a fine calibration. As expected, the neutral pions are expected to be measured up to 45 GeV /c.

The initial study of detector performance and π^0 measurement are crucial for understanding the detectors and any other physics measurements, such as direct photon excess, γ-jet and π^0-jet measurement, flow measurement by photon probes etc. Combing all of these physics measurements, the understanding to the hot-dense matter created at LHC energies will be realized.

Appendix A

Acronyms

ACORDE : ALICE COsmic Ra DEtector

ALICE : A Large Ion Collider Experiment

ALTRO : ALICE TPC ReadOut

AOD : Analysis Object Data

APD : Avalanche Photon Diode

CPV : Charged Particle Veto

CTP : Central Trigger Processor

DAQ : Data Acquisition

DCS : Detector Control System

ECS : Experiment Control System

EM : ElectroMagnetic

EMCAL : ElectroMagnetic CALorimeter

ESD : Event Summary Data

FEE : Frond-End Electronics

HMPID : High Multiplicity Particle Identification Detector

ITS : Inner Tracking System

LED : Light-Emitting Diode

LHC : Large Hadron Collider

MIP : Minimal Ionizing Particle

MRPC : Multi-gap Resistive Plate Chamber

NLO : Next Leading Order

OCDB : Offline Condition DataBase

PHOS : PHoton Spectrameter

pQCD : Perturbative QCD

QA : Quality Assurance

QCD : Quantum ChromoDynamics

QED : Quantum ElectroDynamics

QFT : Quantum Field Theory

RCU : Readout Control Unit

SDD : Silicon Drift Detector

SPD : Silicon Pixel Detector

SSD : Silicon Strip detector

TOF : Time Of Flight

TPC : Time Projection Chamber

TRD : Transition Radiation Detector

TRU : Trigger Readout Unit

ZDC : Zero Degree Calorimeter

Appendix B

Physics performance results

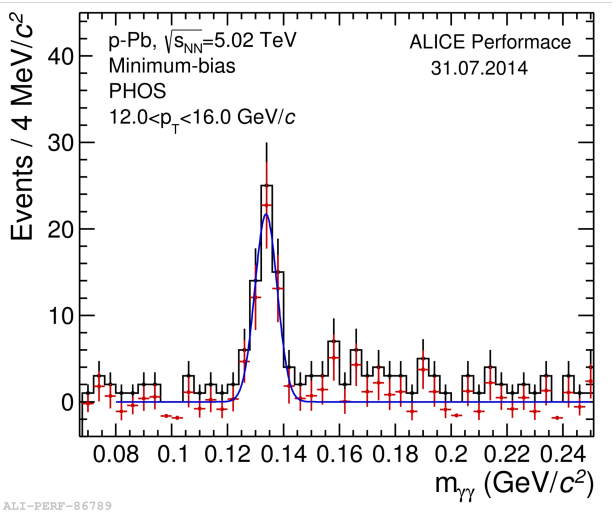

FIGURE B.1: Invariant mass of photon pairs in p-Pb collisions with PHOS at 12-16GeV/c

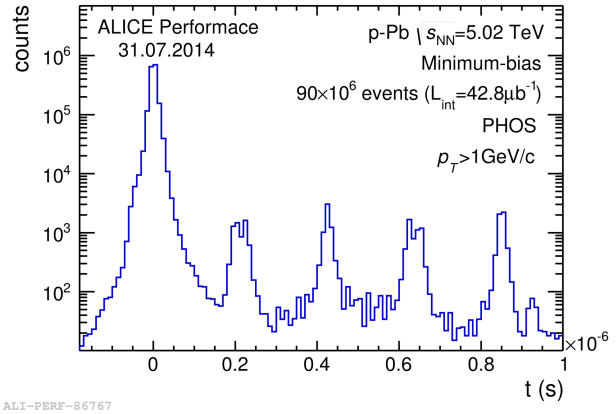

FIGURE B.2: PHOS cluster TOF distribution with transverse momentum $p_{\mathrm{T}} > 1$ GeV/c

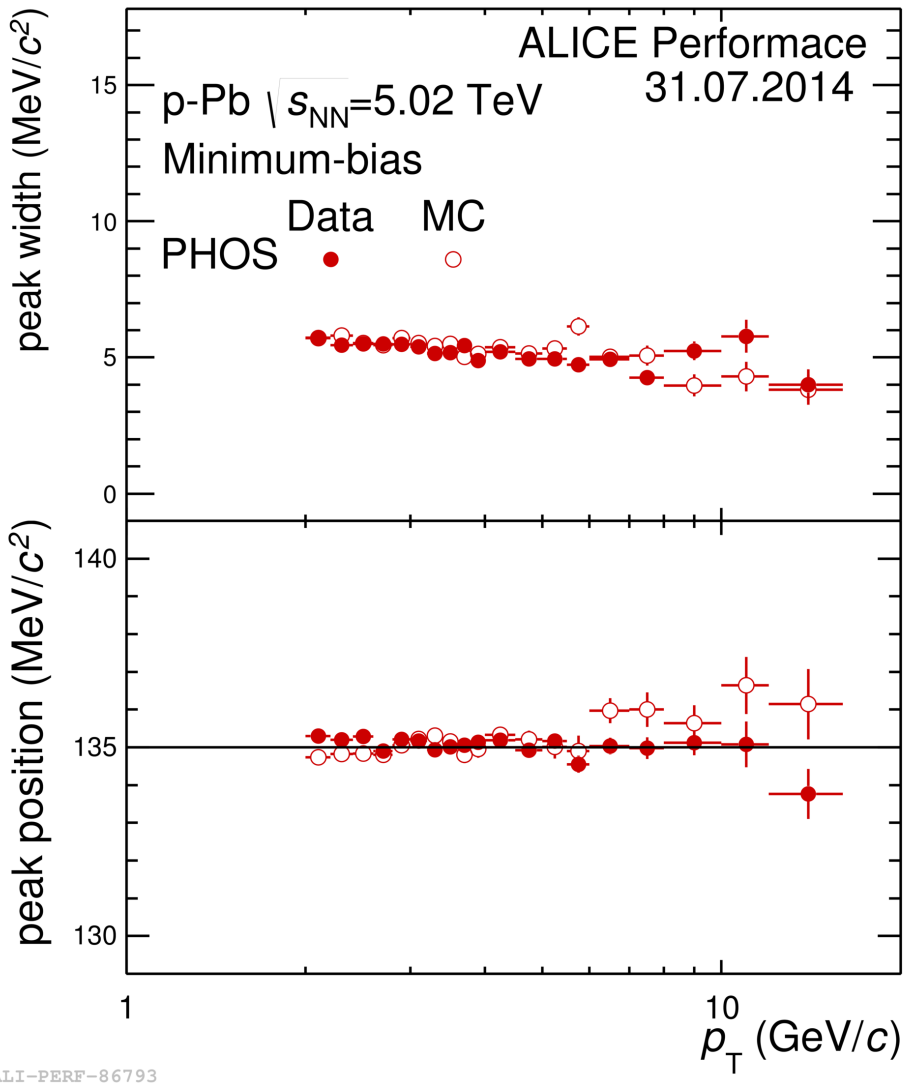

FIGURE B.3: Position (lower) and width (upper) of the π^0 peak on invariant mass spectrum in data and MC.

Bibliography

[1] Lyndon Evans. The LHC machine. *PoS*, EPS-HEP2009:004, 2009.

[2] Georges Aad et al. Observation of a new particle in the search for the Standard Model Higgs boson with the ATLAS detector at the LHC. *Phys.Lett.*, B716:1–29, 2012. doi: 10.1016/j.physletb.2012.08.020.

[3] Chatrchyan et al. Observation of a new boson at a mass of 125 gev with the cms experiment at the lhc. *Physics Letters B*, 716(1):30–61, 2012.

[4] Edward V. Shuryak. Quantum Chromodynamics and the Theory of Superdense Matter. *Phys.Rept.*, 61:71–158, 1980. doi: 10.1016/0370-1573(80)90105-2.

[5] K. Aamodt et al. The ALICE experiment at the CERN LHC. *JINST*, 3:S08002, 2008. doi: 10.1088/1748-0221/3/08/S08002.

[6] S.L. Glashow. Partial Symmetries of Weak Interactions. *Nucl.Phys.*, 22:579–588, 1961. doi: 10.1016/0029-5582(61)90469-2.

[7] Abdus Salam. *Fundamental Theory of Matter; a Survey of Results and Methods.* International Centre for Theoretical Physics, 1968.

[8] Steven Weinberg. A model of leptons. *Physical Review Letters*, 19(21):1264–1266, 1967. doi: 10.1103/PhysRevLett.19.1264.

[9] Mark Srednicki. *Quantum field theory.* Cambridge University Press, 2007.

[10] Günther Dissertori, Ian G Knowles, and Michael Schmelling. *Quantum Chromodynamics, High Energy Experiments and Theory.* Oxford University Press, 2003.

[11] Wikipedia.org: Standard model. URL https://en.wikipedia.org/wiki/Standard_Model.

[12] J.E. Augustin et al. Discovery of a Narrow Resonance in e+ e- Annihilation. *Phys.Rev.Lett.*, 33:1406–1408, 1974. doi: 10.1103/PhysRevLett.33.1406.

[13] Juerg Beringer, JF Arguin, RM Barnett, K Copic, O Dahl, DE Groom, CJ Lin, J Lys, H Murayama, CG Wohl, et al. Review of particle physics. *Physical Review D*, 86(1), 2012.

[14] Kenneth G. Wilson. Confinement of Quarks. *Phys.Rev.*, D10:2445–2459, 1974. doi: 10.1103/PhysRevD.10.2445.

[15] J. Engels, J. Fingberg, K. Redlich, H. Satz, and M. Weber. The Onset of Deconfinement in SU(2) Lattice Gauge Theory. *Z.Phys.*, C42:341, 1989. doi: 10.1007/BF01555877.

[16] V. Goloviznin and H. Satz. The Refractive properties of the gluon plasma in SU(2) theory. *Z.Phys.*, C57:671–676, 1993. doi: 10.1007/BF01561487.

[17] Frithjof Karsch. Lattice results on QCD thermodynamics. *Nucl.Phys.*, A698:199–208, 2002. doi: 10.1016/S0375-9474(01)01365-3.

[18] Sourendu Gupta, Xiaofeng Luo, Bedangadas Mohanty, Hans Georg Ritter, and Nu Xu. Scale for the Phase Diagram of Quantum Chromodynamics. *Science*, 332: 1525–1528, 2011. doi: 10.1126/science.1204621.

[19] A. Gray, I. Allison, C.T.H. Davies, Emel Dalgic, G.P. Lepage, et al. The Upsilon spectrum and m(b) from full lattice QCD. *Phys.Rev.*, D72:094507, 2005. doi: 10.1103/PhysRevD.72.094507.

[20] F. Karsch. Lattice QCD at high temperature and density. *Lect.Notes Phys.*, 583: 209–249, 2002. doi: 10.1007/3-540-45792-5_6.

[21] Michael L. Miller, Klaus Reygers, Stephen J. Sanders, and Peter Steinberg. Glauber modeling in high energy nuclear collisions. *Ann.Rev.Nucl.Part.Sci.*, 57:205–243, 2007. doi: 10.1146/annurev.nucl.57.090506.123020.

[22] Ulrich W. Heinz and Maurice Jacob. Evidence for a new state of matter: An Assessment of the results from the CERN lead beam program. 2000.

[23] G. Agakishiev et al. Low mass e+ e- pair production in 158 AGeV Pb–Au collisions at the CERN SPS, its dependence on multiplicity and transverse momentum. *Phys.Lett.*, B422:405–412, 1998. doi: 10.1016/S0370-2693(98)00083-5.

[24] M.C. Abreu et al. Evidence for deconfinement of quarks and gluons from the J/ψ suppression pattern measured in Pb + Pb collisions at the CERN SPS. *Phys.Lett.*, B477:28–36, 2000. doi: 10.1016/S0370-2693(00)00237-9.

[25] T. Matsui and H. Satz. J/ψ Suppression by Quark-Gluon Plasma Formation. *Phys.Lett.*, B178:416, 1986. doi: 10.1016/0370-2693(86)91404-8.

[26] E. Andersen et al. Strangeness enhancement at mid-rapidity in Pb–Pb collisions at 158 AGeV/c. *Phys.Lett.*, B449:401–406, 1999. doi: 10.1016/S0370-2693(99)00140-9.

[27] Johann Rafelski and Berndt Muller. Strangeness Production in the Quark - Gluon Plasma. *Phys.Rev.Lett.*, 48:1066, 1982. doi: 10.1103/PhysRevLett.48.1066.

[28] Ralf Rapp. Dilepton Spectroscopy of QCD Matter at Collider Energies. *Adv.High Energy Phys.*, 2013:148253, 2013. doi: 10.1155/2013/148253.

[29] R. Albrecht et al. Transverse momentum distributions of neutral pions from nuclear collisions at $\sqrt{s_{NN}}$=200 AGeV. *Eur.Phys.J.*, C5:255–267, 1998. doi: 10.1007/s100520050267.

[30] M.M. Aggarwal et al. Centrality dependence of neutral pion production in 158 AGeV Pb^{-208} + Pb^{-208} collisions. *Phys.Rev.Lett.*, 81:4087–4091, 1998. doi: 10.1103/PhysRevLett.81.4087.

[31] Xin-Nian Wang. Where is the jet quenching in Pb + Pb collisions at 158 AGeV? *Phys.Rev.Lett.*, 81:2655–2658, 1998. doi: 10.1103/PhysRevLett.81.2655.

[32] K. Adcox et al. Suppression of hadrons with large transverse momentum in central Au+Au collisions at $\sqrt{s_{NN}}$ = 130GeV. *Phys.Rev.Lett.*, 88:022301, 2002. doi: 10.1103/PhysRevLett.88.022301.

[33] S.S. Adler et al. Suppressed π^0 production at large transverse momentum in central Au+ Au collisions at $\sqrt{s_{NN}}$ = 200 GeV. *Phys.Rev.Lett.*, 91:072301, 2003. doi: 10.1103/PhysRevLett.91.072301.

[34] J. Adams et al. Transverse momentum and collision energy dependence of high p(T) hadron suppression in Au+Au collisions at ultrarelativistic energies. *Phys.Rev.Lett.*, 91:172302, 2003. doi: 10.1103/PhysRevLett.91.172302.

[35] Javier L. Albacete, Adrian Dumitru, and Cyrille Marquet. The initial state of heavy-ion collisions. *Int.J.Mod.Phys.*, A28:1340010, 2013. doi: 10.1142/S0217751X13400101.

[36] Urs Achim Wiedemann. Jet Quenching in Heavy Ion Collisions. *Landolt-Bornstein*, 23:521–562, 2010. doi: 10.1007/978-3-642-01539-7_17.

[37] Nestor Armesto, Brian Cole, Charles Gale, William A. Horowitz, Peter Jacobs, et al. Comparison of Jet Quenching Formalisms for a Quark-Gluon Plasma 'Brick'. *Phys.Rev.*, C86:064904, 2012. doi: 10.1103/PhysRevC.86.064904.

[38] B.Z. Kopeliovich, J. Nemchik, I.K. Potashnikova, and Ivan Schmidt. Quenching of high-pT hadrons: Energy Loss vs Color Transparency. *Phys.Rev.*, C86:054904, 2012. doi: 10.1103/PhysRevC.86.054904.

[39] J. Nemchik, Iu. A. Karpenko, B.Z. Kopeliovich, I.K. Potashnikova, and Yu. M. Sinyukov. High-pT hadrons from nuclear collisions: Unifying pQCD with hydrodynamics. 2013.

[40] William A. Horowitz. LHC Predictions from an extended theory with Elastic, Inelastic, and Path Length Fluctuating Energy Loss. *Int.J.Mod.Phys.*, E16:2193–2199, 2007. doi: 10.1142/S0218301307007672.

[41] K.H. Ackermann et al. Elliptic flow in Au + Au collisions at $\sqrt{s_{NN}} = 130$ GeV. *Phys.Rev.Lett.*, 86:402–407, 2001. doi: 10.1103/PhysRevLett.86.402.

[42] S. Voloshin and Y. Zhang. Flow study in relativistic nuclear collisions by Fourier expansion of Azimuthal particle distributions. *Z.Phys.*, C70:665–672, 1996. doi: 10.1007/s002880050141.

[43] P. Stankus. Direct photon production in relativistic heavy-ion collisions. *Ann.Rev.Nucl.Part.Sci.*, 55:517–554, 2005. doi: 10.1146/annurev.nucl.53.041002.110533.

[44] A. Adare et al. Enhanced production of direct photons in Au+Au collisions at $\sqrt{s_{NN}} = 200$ GeV and implications for the initial temperature. *Phys.Rev.Lett.*, 104:132301, 2010. doi: 10.1103/PhysRevLett.104.132301.

[45] B. Lenkeit et al. Recent results from Pb–Au collisions at 158 GeV/c per nucleon obtained with the CERES spectrometer. *Nucl.Phys.*, A661:23–32, 1999. doi: 10.1016/S0375-9474(99)85005-2.

[46] Miklos Gyulassy and Xin-nian Wang. Multiple collisions and induced gluon Bremsstrahlung in QCD. *Nucl.Phys.*, B420:583–614, 1994. doi: 10.1016/0550-3213(94)90079-5.

[47] R. Baier, Yuri L. Dokshitzer, Alfred H. Mueller, S. Peigne, and D. Schiff. Radiative energy loss and p(T) broadening of high-energy partons in nuclei. *Nucl.Phys.*, B484:265–282, 1997. doi: 10.1016/S0550-3213(96)00581-0.

[48] Alfred H. Mueller and Jian-wei Qiu. Gluon Recombination and Shadowing at Small Values of x. *Nucl.Phys.*, B268:427, 1986. doi: 10.1016/0550-3213(86)90164-1.

[49] J.W. Cronin, Henry J. Frisch, M.J. Shochet, J.P. Boymond, R. Mermod, et al. Production of Hadrons with Large Transverse Momentum at 200 GeV, 300 GeV, and 400 GeV. *Phys.Rev.*, D11:3105, 1975. doi: 10.1103/PhysRevD.11.3105.

[50] S.S. Adler et al. Common suppression pattern of eta and pi0 mesons at high transverse momentum in Au+Au collisions at $\sqrt{s_{NN}} = 200$ GeV. *Phys.Rev.Lett.*, 96:202301, 2006. doi: 10.1103/PhysRevLett.96.202301.

[51] Betty Bezverkhny Abelev et al. Transverse momentum dependence of inclusive primary charged-particle production in p-Pb collisions at $\sqrt{s_{\mathrm{NN}}} = 5.02$ TeV. *Eur.Phys.J.*, C74(9):3054, 2014. doi: 10.1140/epjc/s10052-014-3054-5.

[52] Thorsten Renk and Kari J. Eskola. Hard dihadron correlations in heavy-ion collisions at RHIC and LHC. *Phys.Rev.*, C84:054913, 2011. doi: 10.1103/PhysRevC.84.054913.

[53] J. Adams et al. Evidence from d + Au measurements for final state suppression of high p(T) hadrons in Au+Au collisions at RHIC. *Phys.Rev.Lett.*, 91:072304, 2003. doi: 10.1103/PhysRevLett.91.072304.

[54] K. Aamodt et al. Particle-yield modification in jet-like azimuthal di-hadron correlations in Pb-Pb collisions at $\sqrt{s_{NN}} = 2.76$ TeV. *Phys.Rev.Lett.*, 108:092301, 2012. doi: 10.1103/PhysRevLett.108.092301.

[55] Michele Arneodo. Nuclear effects in structure functions. *Phys.Rept.*, 240:301–393, 1994. doi: 10.1016/0370-1573(94)90048-5.

[56] Xin-Nian Wang. Systematic study of high p_T hadron spectra in pp, p–a and a–a collisions from sps to rhic energies. *Phys.Rev.C*, 61:064910, 2000.

[57] D. Antreasyan, J.W. Cronin, Henry J. Frisch, M.J. Shochet, L. Kluberg, et al. Production of Hadrons at Large Transverse Momentum in 200 GeV, 300 GeV and 400 GeV pp and pn Collisions. *Phys.Rev.*, D19:764–778, 1979. doi: 10.1103/PhysRevD.19.764.

[58] P.B. Straub, D.E. Jaffe, Henry D. Glass, M.R. Adams, C.N. Brown, et al. Nuclear dependence of high x(t) hadron and high tau hadron pair production in p–A interactions at $\sqrt{s}_{NN} = 38.8$ GeV. *Phys.Rev.Lett.*, 68:452–455, 1992. doi: 10.1103/PhysRevLett.68.452.

[59] Nestor Armesto. Nuclear shadowing. *Journal of Physics G: Nuclear and Particle Physics*, 32(11):R367, 2006.

[60] KJ Eskola, H Paukkunen, and CA Salgado. Eps09—a new generation of nlo and lo nuclear parton distribution functions. *Journal of High Energy Physics*, 2009(04): 065, 2009.

[61] Francois Gelis, Edmond Iancu, Jamal Jalilian-Marian, and Raju Venugopalan. The color glass condensate. *arXiv preprint arXiv:1002.0333*, 2010.

[62] Larry D. McLerran and Raju Venugopalan. Computing quark and gluon distribution functions for very large nuclei. *Phys.Rev.*, D49:2233–2241, 1994. doi: 10.1103/PhysRevD.49.2233.

[63] F. Arleo, P. Aurenche, Fritz W. Bopp, I. Dadic, G. David, et al. Hard probes in heavy-ion collisions at the LHC: Photon physics in heavy ion collisions at the LHC. 2004.

[64] A. Adare et al. Cold Nuclear Matter Effects on J/ψ Yields as a Function of Rapidity and Nuclear Geometry in Deuteron-Gold Collisions at $\sqrt{s_{NN}} = 200$ GeV. *Phys.Rev.Lett.*, 107:142301, 2011. doi: 10.1103/PhysRevLett.107.142301.

[65] Patrick Aurenche, J Ph Guillet, E Pilon, M Werlen, and M Fontannaz. Recent critical study of photon production in hadronic collisions. *Physical Review D*, 73 (9):094007, 2006.

[66] S. Catani, M. Fontannaz, J.P. Guillet, and E. Pilon. Cross-section of isolated prompt photons in hadron hadron collisions. *JHEP*, 0205:028, 2002. doi: 10.1088/1126-6708/2002/05/028.

[67] J. Pumplin, D.R. Stump, J. Huston, H.L. Lai, Pavel M. Nadolsky, et al. New generation of parton distributions with uncertainties from global QCD analysis. *JHEP*, 0207:012, 2002. doi: 10.1088/1126-6708/2002/07/012.

[68] Thomas Peitzmann and Markus H. Thoma. Direct photons from relativistic heavy ion collisions. *Phys.Rept.*, 364:175–246, 2002. doi: 10.1016/S0370-1573(02)00012-1.

[69] H. Arthur Weldon. Simple Rules for Discontinuities in Finite Temperature Field Theory. *Phys.Rev.*, D28:2007, 1983. doi: 10.1103/PhysRevD.28.2007.

[70] Charles Gale and Joseph I. Kapusta. Vector dominance model at finite temperature. *Nucl.Phys.*, B357:65–89, 1991. doi: 10.1016/0550-3213(91)90459-B.

[71] Joseph I. Kapusta, P. Lichard, and D. Seibert. High-energy photons from quark - gluon plasma versus hot hadronic gas. *Phys.Rev.*, D44:2774–2788, 1991. doi: 10.1103/PhysRevD.47.4171,10.1103/PhysRevD.44.2774.

[72] Robert D. Pisarski. Scattering Amplitudes in Hot Gauge Theories. *Phys.Rev.Lett.*, 63:1129, 1989. doi: 10.1103/PhysRevLett.63.1129.

[73] Eric Braaten and Robert D. Pisarski. Soft Amplitudes in Hot Gauge Theories: A General Analysis. *Nucl.Phys.*, B337:569, 1990. doi: 10.1016/0550-3213(90)90508-B.

[74] Rainer J. Fries, Berndt Muller, and Dinesh K. Srivastava. High-energy photons from passage of jets through quark gluon plasma. *Phys.Rev.Lett.*, 90:132301, 2003. doi: 10.1103/PhysRevLett.90.132301.

[75] Simon Turbide, Charles Gale, Sangyong Jeon, and Guy D. Moore. Energy loss of leading hadrons and direct photon production in evolving quark-gluon plasma. *Phys.Rev.*, C72:014906, 2005. doi: 10.1103/PhysRevC.72.014906.

[76] E.D. Courant, M.S. Livingston, and H.S. Snyder. The strong-focusing synchrotron: A new high-energy accelerator. *Phys.Rev.*, 88:1190–1196, 1952. doi: 10.1103/PhysRev.88.1190.

[77] G. Aad et al. The ATLAS Experiment at the CERN Large Hadron Collider. *JINST*, 3:S08003, 2008. doi: 10.1088/1748-0221/3/08/S08003.

[78] S. Chatrchyan et al. The CMS experiment at the CERN LHC. *JINST*, 3:S08004, 2008. doi: 10.1088/1748-0221/3/08/S08004.

[79] Jr. Alves, A. Augusto et al. The LHCb Detector at the LHC. *JINST*, 3:S08005, 2008. doi: 10.1088/1748-0221/3/08/S08005.

[80] G. Dellacasa et al. Alice: technical design report of the dimuon forward spectrometer. 1999.

[81] J. Alme, Y. Andres, H. Appelshauser, S. Bablok, N. Bialas, et al. The ALICE TPC, a large 3-dimensional tracking device with fast readout for ultra-high multiplicity events. *Nucl.Instrum.Meth.*, A622:316–367, 2010. doi: 10.1016/j.nima.2010.04.042.

[82] G. Dellacasa et al. Alice: Technical design report of the time projection chamber. 2000.

[83] G. Dellacasa et al. Alice: technical design report of the inner tracking system (its). 1999.

[84] G. Dellacasa et al. Alice: Technical design report of the transition radiation detector. 2000.

[85] G. Dellacasa et al. Alice: technical design report of the time-of-flight system. 2000.

[86] F. Piuz, W. Klempt, L. Leistam, J. De Groot, and J. Schükraft. Alice high- momentum particle identification: Technical design report. 1998.

[87] P. Cortese et al. Alice technical design report on forward detectors: Fmd, t0 and v0. 2004.

[88] P. Cortese et al. Alice electromagnetic calorimeter technical design report. 2008.

[89] G. Dellacasa et al. Alice technical design report of the photon spectrometer (phos). 1999.

[90] J. Allen et al. Alice dcal: An addendum to the emcal technical design report di-jet and hadron-jet correlation measurements in alice. 2010.

[91] P. Cortese et al. Alice: Physics performance report, volume i. *J. Phys. G-Nucl. Part. Phys.*, 30(11):1517–1763, November 2004. ISSN 0954-3899. doi: 10.1088/0954-3899/30/11/001.

[92] B. Alessandro et al. Alice: Physics performance report, volume ii. *J. Phys. G-Nucl. Part. Phys.*, 32(10):1295–2040, October 2006. ISSN 0954-3899.

[93] ALICE collaboration et al. Performance of the alice experiment at the cern lhc. *International Journal of Modern Physics A*, 2014.

[94] DV Aleksandrov, SF Burachas, MS Ippolitov, VA Lebedev, VI Manko, SA Nikulin, AS Nyanin, IG Sibiriak, AA Tsvetkov, AA Vasiliev, et al. A high resolution electromagnetic calorimeter based on lead-tungstate crystals. *Nuclear Instruments and Methods in Physics Research Section A: Accelerators, Spectrometers, Detectors and Associated Equipment*, 550(1):169–184, 2005.

[95] Zhong-Bao Yin and Dai-Cui Zhou. Performance of the alice phos front-end electronics. *HEP & NP*, 30(12), 2006.

[96] H. Muller, R. Pimenta, L. Musa, Z.B. Yin, D. Rohrich, et al. Trigger electronics for the ALICE PHOS detector. *Nucl.Instrum.Meth.*, A518:525–528, 2004. doi: 10.1016/j.nima.2003.11.076.

[97] N Ahmad et al. Alice technical proposal. *CERN/LHCC*, pages 95–71, 1995.

[98] Aliphysicsselection. URL http://aliroot-docs.web.cern.ch/aliroot-docs/AliPhysicsSelection.html.